This is a preprint, the final version is subject to change, of the American Mineralogist (MSA)
Cite as Authors (Year) Title. American Mineralogist, in press.
DOI: https://doi.org/10.2138/am-2019-6811

REVISION 1

Origin of vesuvianite-garnet veins in calc-silicate rocks from part of the Chotanagpur Granite Gneiss Complex, East Indian Shield: the quantitative P-T-X_{CO2} topology in parts of the system CaO-MgO-Al_2O_3-SiO_2-H_2O-CO_2 (+Fe_2O_3, F)

Anindita Dey[1]*, Sirina Roy Choudhury[1], Subham Mukherjee[1], Sanjoy Sanyal[1], Pulak Sengupta[1]

[1]Department of Geological Sciences, Jadavpur University, Kolkata 700032, India

*correspondence: E-mail: deyanindita.ju@gmail.com; Telephone: +91 033-24572740

ABSTRACT

A calc-silicate rock from part of the Chotanagpur Granite Gneiss Complex (CGGC), East India, develops veins and patches of vesuvianite (F: 2.3-3.9 apfu, Fe^{3+}: 1.7-2.1 apfu) and garnet ($Gr_{71-80}Alm_{12-17}Adr_{1-9}$) proximal to amphibole-bearing quartzo-feldspathic pegmatitic veins. The host calc-silicate rock exhibits a prominent gneissic banding that is defined by alternate clinopyroxene- and plagioclase rich layers. The vesuvianite-garnet veins are both parallel and cross-cutting the gneissic banding of the host calc-silicate rock. Two contrasting mineralogical domains that are rich in garnet and vesuvianite respectively develop within the vesuvianite-garnet veins. Textural studies support the view that the garnet- and vesuvianite-rich domains preferentially develop in the clinopyroxene- and plagioclase-rich layers of the host calc-silicate rocks respectively. Some of the vesuvianite-rich domains of the veins develop the assemblage vesuvianite + quartz + calcite +anorthite (as a result of the reaction diopside + quartz + calcite + anorthite = vesuvianite) which was deemed metastable in the commonly used qualitative isobaric T-X_{CO2} topology in the system CaO-MgO-Al_2O_3-SiO_2-H_2O-CO_2 (CMASV).

Using an internally consistent thermodynamic database, quantitative petrogenetic grids in the P-T and isobaric T-X_{CO2} spaces have been computed in the CMASV system. The influence

of the non CMASV components (e.g. Na, Fe^{3+}, F) on the CMASV topologies have been discussed using the published a-X relations of the minerals. Our study shows topological inversion in the isobaric T-X_{CO2} space which is primarily dependent upon the composition of the vesuvianite. The quantitative CMASV topologies presented in this study successfully explain the stabilities of the natural vesuvianite-bearing assemblages including the paradoxical assemblage vesuvianite + quartz + calcite + anorthite.

Application of the activity-corrected CMASV topology suggests that infiltration of F-bearing oxidizing aqueous fluids into the calc-silicate rocks develop the vesuvianite-garnet veins in the studied area. A genetic link between quartzo-feldspathic pegmatites and the vesuvianite-garnet veins seems plausible.

This study demonstrates controls of topological inversion in the complex natural system, owing to which, certain mineral assemblages that are deemed metastable in one set of reaction geometry, develop in nature.

Keywords: calc-silicate rocks, vesuvianite, CMASV petrogenetic grid, fluorine infiltration, topological inversion

INTRODUCTION

Vesuvianite (previously known as 'Idocrase') is a rare mineral that is found in contact metamorphic aureoles, regionally metamorphosed calcareous rocks, rodingites and altered nepheline syenites (Arem 1973; Hochella et al. 1982; Rice 1983; Valley et al. 1985; Ahmed-Said and Leake 1996; Bogoch et al. 1997; Galuskin et al. 2003; Zanoni et al. 2016). Studies have shown that in terms of ordering and symmetry, the high temperature (>400°C) vesuvianites that are found at contact metamorphic aureoles can be distinguished from the vesuvianites that formed in low temperature (<300°C) metasomatic processes (Allen and Burnham 1992; Elmi et

al. 2011). Although majority of the workers reported vesuvianite from low pressure (<2 kbar) assemblages (Labotka et al. 1988; Cartwright and Oliver 1994; Ahmed-Said and Leake 1996; Johnson et al. 2000; Nabelek and Morgan 2012; Nabelek et al. 2013 among others), its occurrence in higher pressure rocks has also been encountered by many workers (Palache 1935; Tracy et al. 1978; Valley and Essene 1979; Valley et al. 1985; Bogoch et al. 1997; Halama et al. 2013 among others). The structural formula, the site distribution of cations and anions and most importantly, the stability of vesuvianite have been a subject of considerable debate (Hochella et al. 1982; Valley et al. 1985; Hoisch 1985; Groat et al. 1992a, 1992b, 1994, Armbruster and Edwin 2000b, 2000a; Balassone et al. 2011; Elmi et al. 2011; Ogorodova et al. 2011; Panikorovskii et al. 2017). Studies have shown that vesuvianite-bearing rocks may be a monitor of the metamorphic fluid flow over a range of pressure and temperature (Valley et al. 1985 among others). However, the reaction topologies of the vesuvianite-bearing assemblages are not properly understood. Contrasting topologies (majorly qualitative) have been proposed in the isobaric T-X_{CO2} space in the system CaO-MgO-Al_2O_3-SiO_2-mixed volatile/H_2O-CO_2 (CMASV; Kerrick et al. 1973; Valley et al. 1985). The main discrepancy of the previous studies seems to be related to the lack of precise thermodynamic data for many critical vesuvianite bearing reactions that serve as the major hindrance for construction of quantitative topologies in the system CMASV. Absence of quantitative CMASV topologies also put constraints on evaluating the effects of non-CMASV components on the stabilities of vesuvianite-bearing assemblages in natural rocks.

Valley et al. (1985) on the basis of their structural refinement studies of a naturally occurring vesuvianite sample proposed a site distribution scheme and a structural formula for the mineral that has been corroborated by subsequent crystallochemical studies (Hoisch 1985;

Labotka et al. 1988; Ahmed-Said and Leake 1996). These authors also presented a qualitative isobaric T-X_{CO2} topology in the CMASV system and predicted the optimum thermal stabilities of different vesuvianite-bearing assemblages over a range of X_{CO2}. Although the topology of Valley et al. (1985) explains the petrological evolutions of most of the naturally occurring vesuvianite–bearing rocks, it cannot explain the stability of the critical assemblage vesuvianite + quartz + calcite +anorthite (linked with the reaction diopside + quartz + calcite + anorthite = vesuvianite) that is reported by several other workers (Hover Granath et al. 1983; Tracy and Frost 1991; Cartwright and Oliver 1994).

Against this back drop we report the occurrence of the critical mineral assemblage vesuvianite + quartz + calcite + anorthite from a calc-silicate rock from the Chotanagpur Granite Gneiss Complex (CGGC) of the East Indian shield. Quantitative petrogenetic grids in P-T (for fixed X_{CO2}) and T-X_{CO2} (isobaric) spaces have been constructed in parts of the system CMASV using the internally consistent thermodynamic data of Holland and Powell (1998, revised 2002). The effects of non-CMASV components on the vesuvianite-bearing topologies in the simple CMASV system have been quantitatively evaluated using the published a-X relations of the relevant minerals. Based on these, our study demonstrates that the isobaric T-X_{CO2} topology of the vesuvianite–bearing assemblages depends largely on the activities of the minerals, particularly on the activity of vesuvianite. The quantitative petrogenetic grids (isobaric T-X_{CO2}) that are proposed in this study explain the stability of the natural assemblage vesuvianite + quartz + calcite + anorthite that was deemed metastable in the T-X_{CO2} topology of Valley et al. (1985). Combining the calculated petrogenetic grid and the reaction textures obtained from the studied rock, it is inferred that an infiltration driven metamorphism (by F-bearing oxidizing aqueous

fluids) was responsible for the stability (and instability) of the vesuvianite bearing assemblages in the studied area.

GEOLOGICAL BACKGROUND

The CGGC covers around 80,000 km^2 area in east-central India and constitutes a major portion of the Precambrian Indian shield (Fig. 1a). The geology and geochronology of the CGGC has been reviewed in detail by Mukherjee et al. (2019) and only a brief summary will be discussed here. Vast swathes of felsic orthogneisses (including porphyritic and migmatitic varieties) of varying ages constitute the country rock of the terrane and host enclaves of pelitic, calc-silicate and meta-mafic granulites of various dimensions (cm to km scale). The quartzite-metapelites-metacarbonate rocks have been shown to be the metamorphic equivalent of the sedimentary ensemble of sandstone-shale-limestone (Dey et al. 2017). U-Pb zircon and Pb-Pb galena ages reveal that the protoliths of these metapelitic units were deposited between ~1700 and 1650 Ma (Singh et al. 2001; Dey et al. 2017) possibly over a Paleoproterozoic felsic crust of ~1750-1650 Ma (Chatterjee and Ghose 2011; Dey et al. 2017; Saikia et al. 2017). Subsequently the sediments were deformed and metamorphosed (M_1-D_1) in medium pressure ultra-high to high temperature granulite facies conditions at ~1650 Ma (Sanyal and Sengupta 2012; Dey et al. 2017). The terrane experienced multiple magmatic events during Mesoproterozoic (anorthosite magmatism during ~1550 Ma: Chatterjee et al. 2008; felsic magmatism during ~1450 Ma: Mukherjee et al. 2017, 2018) which was followed by an extensive high pressure granulite grade metamorphism (~750-825°C, 9-14 kbar; Karmakar et al. 2011; Mukherjee et al. 2017; Chatterjee 2018) and deformation (M_2-D_2) during Stenian-Tonian time (Maji et al. 2008; Chatterjee et al. 2010; Karmakar et al. 2011; Rekha et al. 2011; Mukherjee et al. 2017). A suite of mafic dykes intruded the country rock after the D_2 deformation. The eastern part of the CGGC records

115 another phase of strong deformation event (M_3-D_3) at ~920-880 Ma; this deformation is
116 responsible for the intense folding of the early foliations and mafic dykes and generation of a
117 prominent N-S trending foliation (Chatterjee 2018; Mukherjee et al. 2018b). The metamorphism
118 accompanying this latest deformation event corresponds to amphibolite facies conditions (Ray et
119 al. 2011; Mukherjee et al. 2018b).

120 The studied calc-silicate rocks occur as enclaves within the Mesoproterozoic felsic
121 orthogneiss (~1450 Ma; Mukherjee et al. 2018a) in the north-eastern part of the CGGC near
122 Deoghar (Fig. 1a). Metasedimentary (quartzite-metapelite-calc-silicate) and metabasic rocks and
123 augen gneiss occur as enclaves within the felsic country rock that is subsequently intruded by
124 mafic dykes and quartzo-feldspathic pegmatitic veins (Fig. 1b). Similar to its metapelitic
125 counterpart, majority of the metamorphosed calcareous supracrustals exhibit granulite grade
126 mineral assemblages (garnet-clinopyroxene-plagioclase±scapolite). Locally the calc-silicate
127 rocks contain epidote ± zoisite ± vesuvianite ± wollastonite (Patel 2007; Sanyal and Sengupta
128 2012). The most pervasive planar structure recorded in the study area is depicted by a N-S planar
129 fabric developed in all the lithologies and inferred to be the product of the last major
130 tectonothermal event (M_3-D_3) in the area (Mukherjee et al. 2017, 2018b, 2019). Multiple
131 generations of quartzo-feldspathic pegmatitic veins intruded the host as well as the enclave suite
132 of rocks. One group of these veins exhibits folding in response to the D_3 deformation, while the
133 other group is undeformed and cuts across the earlier fabrics.

134 **FIELD OCCURRENCES**

135 The isolated outcrops of the studied calc-silicate rocks occur within a thick soil cover and
136 show no direct contact with the felsic orthogneiss. The latter rock, however, is exposed only a
137 few tens of meters away. From the overall distribution of rocks in the area, it is presumed that the

studied calc-silicate rocks occur as enclaves within the felsic orthogneiss. Occurrences of calc-silicate pods within felsic orthogneiss have also been documented from neighboring areas (Bhattacharya 1976; Patel 2007; Roy Choudhury et al. 2016). The studied calc-silicate rocks show mm to cm thick alternate layers rich in plagioclase and clinopyroxene (Fig. 2a). The compositional layering can be traced in the individual outcrops and has a N-S trend which is also recorded in the adjoining felsic orthogneiss (Mukherjee et al. 2017). In places, the thicker clinopyroxene bands become discontinuous and exhibit pinch and swell or boudin structures.

The vesuvianite-garnet bearing assemblages occur as discontinuous veins and patches within the calc-silicate rocks. Commonly, the veins are roughly parallel to the gneissic banding of the host rock, but they also dissect the latter in places (Fig. 2b). These veins are composed of aggregates of garnet, clinopyroxene, plagioclase and light green colored vesuvianite (Fig. 2b-c). Gradual variation from garnet-rich to vesuvianite- rich zones is a common feature in the veins (Fig. 2b). The garnet and vesuvianite-rich parts of the veins preferentially develop in the clinopyroxene- and plagioclase-rich layers of the host calc-silicate rock respectively (Fig. 2c-d). Locally, these veins mimic the structures defined by the layers of the host calc-silicate rock (Fig. 2d). The boundary between the vesuvianite-garnet veins and the host rock shows mineralogical gradation (Fig. 2b). These veins are invariably associated with amphibole bearing quartzo-feldspathic pegmatitic veins. Similar to the vesuvianite-garnet veins, the pegmatitic veins also intrude along or locally cut across the compositional bands of the calc-silicate rock (Fig. 2e). The border between the pegmatite and the calc-silicate rock is commonly marked by distinct amphibole rich selvages (Fig. 2f). Proximal to the pegmatitic veins, the calc-silicate rock develops amphibole, the modal proportion of which decreases away from the veins.

PETROGRAPHY AND MINERAL COMPOSITIONS

Analytical methods

Petrography. Several thin sections that are cut parallel and perpendicular to the veins are studied by standard petrographic microscopy.

Mineral compositions. Compositions of minerals were analyzed with a CAMECA SX5 microprobe at the Central Research Facility of the Indian Institute of Technology (Indian School of Mines), Dhanbad, India. Operating conditions were 15kV accelerating voltage and 15nA beam current, with a beam diameter of 2-3 μm. Well characterized natural and synthetic standards were used to calibrate the instrument for the measurement of the concentration of the major elements (details in Supplemental Table 1a). During cation recalculation from oxide weight percentage, Fe^{+3} was calculated after the scheme of Droop (1987) and Grew et al. (2013) except vesuvianite, where all Fe was considered to be in Fe^{+3} state (see mineral composition of vesuvianite for more details). Anions of vesuvianite were calculated following the procedure described by Ketcham (2015). Cation calculation of amphibole was according to the scheme of Leake et al. (1997, 2004). Few representative analyses of the minerals are presented in Tables 1-3; expanded tables have been given as supplemental materials (Supplemental Table 1b-g). The mineral abbreviations of Kretz (1983) are used in the figures and tables.

Salient micro-textural and compositional attributes of the host calc-silicate rocks, the quartzo-feldspathic pegmatitic veins and the vesuvianite-garnet veins are presented below.

Host calc-silicate rock

The host calc-silicate rock is composed of plagioclase (Pl) + clinopyroxene (Cpx) + titanite (Ttn) ± quartz (Qtz) ± apatite (Apt) ± amphibole (Am). Millimeter thick layers alternatively rich in clinopyroxene and plagioclase are the characteristic features of the rock (Fig. 3a). Together, the clinopyroxene + plagioclase constitute >80 vol% of the rock. The plagioclase

and clinopyroxene grains show polygonal grain boundaries that define a granoblastic mosaic. Locally, clinopyroxene and plagioclase grains are stretched to impart a foliation (Fig. 3b). The clinopyroxene grains contain inclusions of quartz and titanite (Fig. 3a). Plagioclase contains abundant inclusions of quartz. Proximal to pegmatitic veins, the clinopyroxenes are replaced by amphibole (Fig. 3c). Titanite is randomly dispersed in the rock as an accessory phase (Fig. 3a-c).

The clinopyroxene grains are compositionally homogeneous with a restricted X_{Mg} ($Mg/Mg+Fe_T$) varying within 0.58-0.63 (Fig. 4a; Table 1). The aegerine and donpeacorite [$(Mn,Mg)MgSi_2O_6$] component together do not exceed 2 mol%. The Al content of clinopyroxene does not exceed 0.06 apfu (atoms per formula unit) with negligible Fe^{+3}(calculated from charge balance technique).

The plagioclase grains have a wide compositional range of An_{59-91} Ab_{40-9} Or_{1-0} (Fig. 4b; Table 2).

The titanite grains contain a significant amount of Al_2O_3 (ranging between 6.8-9.6 wt%) and fluorine (1.7-2.5 wt%) and Al (0.25-0.36 apfu) in titanite is negatively correlated with Ti (0.63-0.73 apfu) (Table 2).

The amphiboles that replace clinopyroxene have compositions that straddle the fields of pargasite and edenite (Fig. 4c; Table 1). No compositional zoning is noted within individual amphibole grains.

Quartzo-feldspathic pegmatitic veins

The pegmatitic veins are composed of coarse grained plagioclase, quartz and amphibole showing interlocking texture (Fig. 3d). The minerals do not show any evidence of internal deformation or recrystallization. Rarely, small individual grains of clinopyroxene are found trapped within the interlocking mosaic (Fig. 3d). Large prismatic amphibole grains are dispersed

randomly in a matrix of quartz and plagioclase (Fig. 3e). Near the boundary of the pegmatitic vein, locally these amphiboles replace the clinopyroxene grains of the host calc-silicate rock. Adjacent to the amphiboles, the twinned plagioclase (Pl_1) grains of the pegmatitic veins are variably replaced by randomly oriented micro-veins or patches of optically homogeneous plagioclase (Pl_2, Fig. 3f).

Two generations of plagioclase have contrasting composition. The texturally older Pl_1 ($An_{77-62}Ab_{22-37}Or_{<1}$) is less albitic than the texturally younger Pl_2 ($An_{58-16}Ab_{82-42}Or_{<2}$) (Fig. 4b; Table 2). Compositional range of Pl_1 overlaps with the composition of plagioclase in the host calc-silicate rocks (Fig. 4b).

Amphibole grains are compositionally homogeneous and its compositions are plotted in the fields of pargasite to ferro-pargasite to ferro-edenite (Fig. 4c; Table 1). The Fe^{+3} and Na content of amphiboles do not exceed 0.3 and 0.4 apfu respectively.

Vesuvianite-garnet veins

The veins show mm-thick segregations (henceforth 'domains') rich in vesuvianite (Ves) or garnet (Grt) which will be hereafter termed as domain A and B respectively (Fig. 3g-h). The two domains do not show any significant variation in mineral assemblage but there are significant differences in the modal abundances of the minerals. The modal ratios of plagioclase to clinopyroxene to vesuvianite to garnet in domain A and domain B are 50:15:25:10 and 10:25:5:60 respectively. In domain B, amount of vesuvianite is less and it is only restricted to a few micro-domains. On the basis of the presence or absence of vesuvianite, domain B is further divided into two distinct subdomains B1 and B2 (Fig. 3g-h). Salient petrographical features of these mineralogically distinct domains and subdomains are presented below.

229 **Domain A: Vesuvianite-rich domains.** These domains preferentially develop in the
230 plagioclase rich layers of the host calc-silicate rock. Polygonal aggregates of plagioclase and
231 clinopyroxene with minor titanite forms a granoblastic mosaic (Fig. 3i-j). Subhedral vesuvianite
232 grains grow over this mosaic and variably engulf clinopyroxene and plagioclase (Fig. 3k-m). The
233 vesuvianites do not show evidence of internal strain. Inclusions of quartz, titanite, apatite and
234 rare calcite are present in vesuvianite (Fig. 3k-m). Volumetrically minor (<10 vol%) garnet
235 occurs in two modes. Commonly, in domains devoid of quartz, small grains of garnet are
236 included in vesuvianite (Fig. 3k-l). In the second mode, coronal garnet separates clinopyroxene
237 from plagioclase (Fig. 3k-l, n).
238 Variation in the thickness of the coronal garnet and the modal ratio of garnet and
239 vesuvianite are noted. Locally, domain A with a few thin (50-100 μm) garnet coronas grades into
240 domain B rich in thick (>1 mm) subhedral garnet grains through an intermediate zone where the
241 thickness of the garnet coronas increases to produce a sieve texture (Fig. 3g-h).
242 **Domain B: Garnet-rich domains.** Two distinct subdomains have been identified within
243 this garnet-rich domain.
244 Domain B1: Vesuvianite-free garnet-rich domains: Here large volumes of small
245 subhedral garnet grains form a network with clinopyroxene, subordinate titanite, plagioclase, rare
246 calcite and quartz occurring within the interstitial spaces. The network of garnet surrounds
247 clinopyroxene and separates them from plagioclase. Protrusions of garnet into clinopyroxene and
248 plagioclase are common feature. All the textural features of this domain are presented in Fig. 3o-
249 p.
250 Domain B2: Vesuvianite-bearing garnet-rich domains: This subdomain is restricted to
251 near the boundary of domain B proximal to domain A (Fig. 3g-h). Except for the presence of

stumpy vesuvianite grains in the clinopyroxene-rich matrix (Fig. 3q), this domain is texturally similar to domain B1. Network of garnet aggregates surround clinopyroxene, vesuvianite, plagioclase, titanite, rare calcite and quartz (Fig. 3q). The boundary of garnet with clinopyroxene and plagioclase is sutured. Vesuvianite on the other hand, shares straight boundaries with the surrounding garnet (Fig. 3q). Similar to domain A, two or more phases amongst plagioclase, clinopyroxene, quartz/garnet, titanite, calcite and apatite are noted as inclusions within vesuvianite.

Despite the large modal variation, no significant compositional variation has been noted between the minerals that constitute domain A and B. Composition of vesuvianite has been recalculated on the basis of 50 cations (after the structural formula $Ca_{19}Mg_2Al_{11}Si_{18}O_{69}(OH)_9$ of Valley et al. 1985, following the site occupancy scheme described by Hoisch (1985), Groat et al. (1994), Ahmed-Said and Leake (1996)). Compositionally homogeneous vesuvianite shows significant F (1.5-2.5 wt% ; 2.3-3.9 apfu) with insignificant Cl content (from below detection limit of EPMA to 0.2 wt%) in its structure (Table 3). The Si content is always >17.8 apfu suggesting that very little to no Al is present in its T site (Groat et al. 1992a). The Al content of vesuvianite (15.6-16.8 wt% Al_2O_3, 9-10 Al apfu) requires that all the Fe to be in its ferric state to balance the charge (Groat et al. 1992a). Fe_2O_3 equivalent to the measured FeO varies between 4.5-5.5 wt% (equivalent to 1.7-2.1 apfu Fe^{+3}). The Al/Al+Fe^{+3} ratios vary between 0.82-0.85 (Table 3). Presence of 1.4-1.5 apfu Mg (1.8-2 wt%) suggests that the bivalent Y1 site (occupancy 1 apfu; Hoisch 1985; Ahmed-Said and Leake 1996) is solely occupied by Mg with no Fe^{+2}. However, according to more recent studies (Elmi et al. 2011), the occupancy of Y1 site is limited and it never exceeds 0.5. The excess Mg fills the Y3 site along with Mn, Fe^{+3}, Al^{+3} and Ti^{+4} (Hoisch 1985; Groat et al. 1992a; Ahmed-Said and Leake 1996). Presence of 33-34 wt% CaO

(17.9-18.2 apfu Ca) results in incomplete filling up of the X site (Ca site with occupancy 19 apfu; Hoisch 1985; Groat et al. 1992a). The Na content never exceeds 0.2 apfu. The sum of the octahedrally coordinated cations (Y site cations) always exceed 13 apfu indicating the existence of excess Al and Fe^{+3} in the T1 site (Groat et al. 1994; Ahmed-Said and Leake 1996; Elmi et al. 2011). All the vesuvianites are boron-free (B is less than 20 ppm or even less than the detection limit i.e. 2 ppm of LA-ICP-MS) which indicates that the T2 sites are essentially empty (Groat et al. 1994; Elmi et al. 2011).

No compositional difference was observed between the garnet inclusions in vesuvianite and the coronal garnets from domain A and B. The garnet is dominated by grossular (71-80 mol%) with small and variable almandine (12-17 mol%) and andradite (1-9 mol%) components (Table 3). Pyrope and spessartine contents are low (together they never exceed 4 mol%). The garnets contain considerable amounts of F (0.4 -1 wt%) with an average of 0.6 wt% (Table 3). Similar high value of F (up to 0.76 wt%) in garnets from vesuvianite bearing calc-silicate rocks are also reported by Valley et al. (1983). No compositional zoning is observed within individual garnet grains.

The X_{Mg} [$Mg/(Mg+Fe^{2+})$] of clinopyroxene ranges between 0.54-0.58 (Fig. 4a). The aegerine, jadeite, tschermak and donpeacorite components altogether do not exceed 6 mol% (Table 1). Amount of Al is restricted between 0.08-0.1 apfu with negligible content of Fe^{+3}. No zoning in terms of Fe–Mg distribution is noted within the individual grains.

The plagioclase is highly calcic ($An_{94-97}Ab_{3-6}$; Fig. 4b; Table 2) and shows no compositional zoning; the orthoclase component is negligible.

Titanite has significant compositional variations in terms of Al_2O_3 and F. In both the domains (domain A and B) Al_2O_3 and F varies between 8-12 wt% and 2-3.5 wt% respectively

298 (Table 2). A negative correlation is observed between the Al (0.31-0.43 apfu) and Ti content
299 (0.56-0.67 apfu).

300 The apatite contains upto 5 wt% of F in its structure.

301 **EVOLUTION OF MINERAL ASSEMBLAGE (HOST CALC-SILICATE ROCK TO**
302 **VESUVIANITE-GARNET VEINS)**

303 Textural relations and composition of minerals attest to chemical reactions for formation
304 of the vesuvianite-garnet veins. The major phases found in the different domains of the calc-
305 silicate rocks can be represented in the system $CaO–Na_2O–FeO–MgO–Al_2O_3–Fe_2O_3–SiO_2–F-$
306 $(CO_2–H_2O)$. Since titanite is the only effective Ti-bearing phase, presence of titanite will not
307 influence the CMASV topology. For this reason, TiO_2 is not considered as a system component.
308 In this complex system, mineral reactions deduced from textural criteria are multivariate. The
309 mineralogical evolution of the vesuvianite-garnet veins can be traced from the stabilization of the
310 inclusion assemblage clinopyroxene + plagioclase ± garnet ± quartz ± calcite. Based on the
311 presence of the inclusion assemblage of clinopyroxene, plagioclase, calcite and garnet in
312 vesuvianite in both domain A and domain B2 it is proposed that vesuvianite grew at the expense
313 of these minerals by the following reactions:

314 $Cpx + Grt + Cal + Pl + H_2O + F \pm O_2 \rightarrow Ves + CO_2$ (i)

315 The vesuvianite grains that contain inclusions of quartz rather than garnet are assumed to be the
316 products of the reaction:

317 $Cpx + Qtz + Cal + Pl + H_2O + F \pm O_2 \rightarrow Ves + CO_2$ (ii)

318 As F is present in the vesuvianite composition and no mineral on the reactant side contain
319 substantial amount of F, it is added as a free phase in the reactant side in both the reactions. In
320 reaction (i), the andradite component in garnet may contribute to the Fe^{+3} present in the

vesuvianites. An increase in fO_2 condition may be another possible mechanism in reaction (i) and the only possible mechanism in reaction (ii) that can account for the ferric ion in the vesuvianite.

In domain A and B, formation of garnet corona around plagioclase, quartz and clinopyroxene may be explained by the reaction:

$$Pl + Cal + Cpx + Qtz \pm O_2 \rightarrow Grt + CO_2 \qquad \text{(iii)}$$

Clinopyroxenes do not have an essenite component, so oxidation of hedenbergite through oxygenated fluid influx (increased fO_2 condition) is one possible mechanism that could explain the production of an andradite component in garnet (Sengupta et al. 1997).

In domain A and B2, garnet forms corona (usually inferred as a disequilibrium texture) over vesuvianite, and at the same time they share straight grain boundaries (equilibrium texture) which demands explanation. The straight non-interfering grain boundary between these two minerals suggests that the coronal garnet formed in the stability field of vesuvianite and during its growth it utilized the space around vesuvianite. That is, after the formation of vesuvianite, vesuvianite-garnet became the stable assemblage and the vesuvianite grains allowed passive growth of garnet corona without being involved in the reaction.

Hence, the inferred reactions stated above predict the following sequence of mineralogical change:

Plagioclase + clinopyroxene ± quartz ± calcite (host calc-silicate rock) → Plagioclase + clinopyroxene + garnet + quartz ± calcite (inclusion assemblage) → vesuvianite-bearing assemblage → vesuvianite + coronal garnet-bearing assemblage

342 The last two constitute the vesuvianite-garnet vein. The textural features suggest that the
343 minerals, which constitute the vein, grew in situ by replacement of a pre-existing assemblage.
344 Hence, it is most likely that the 'vein', here, do not represent an intrusive rock. Rather, it
345 represents the channels of fluid infiltration and metasomatism.

346 The negative correlation between Al and Ti indicates the reaction Ti + O →
347 $(Al/Fe)^{3+}$+ (F/OH). Several studies presumed that pressure is the only variable that dictates
348 the entry of Al in the structure of titanite (Smith 1981; Franz and S. Spear 1985; Enami et
349 al. 1993; Troitzsch and Ellis 2002). Subsequent studies, however, demonstrate that bulk
350 rock compositions and fugacities of CO_2, H_2O and F exert strong influence and may even
351 offset the influence of pressure on the entry of Al and F in the titanite structure (Markl and
352 Piazolo 1999; Sengupta et al. 2004). Sengupta et al. (2004) showed that the formation of
353 aluminous titanite is favored by a decrease in fCO_2 and that aluminous titanite can occur at
354 pressures even below 5 kbar if the ambient fluids are rich in H_2O (and have low fCO_2).

355 **P-T CONDITION OF FORMATION OF THE VESUVIANITE-GARNET VEINS**

356 Vesuvianite is a hydrous phase. Hence, P-T stability of vesuvianite-bearing assemblages
357 is strongly dependent upon the fluid compositions. The charge balance constraint suggests that
358 the garnet composition of the vesuvianite-garnet veins is a solid solution of grossular-almandine-
359 andradite with marginally small amount of pyrope. In absence of significant Fe^{2+}/Mg in the
360 garnet, the pressure and temperature conditions cannot be constrained with garnet-
361 clinopyroxene-plagioclase-quartz assemblage (Ellis and Green 1979). The field occurrences
362 of the studied rocks show that the vesuvianite-garnet veins always develop close to the
363 amphibole-plagioclase bearing pegmatitic veins and thus suggest a genetic link between the two.
364 For this reason, amphibole–plagioclase thermobarometers are used to constrain the P-T condition

365 of formation of the vesuvianite veins as well as the pegmatites. The amphiboles and the albitic
366 plagioclase (Pl_2) are always closely associated and both replace the primary assemblage of the
367 host calc-silicate rock. In view of that, the second generation plagioclase (Pl_2) is considered to be
368 in equilibrium with amphibole and is used for the P-T calculations. Supplemental table 2 shows
369 the results of P-T calculations with different geothermobarometric formulations (Holland and
370 Blundy 1994; Anderson and Smith 1995) involving amphibole and plagioclase. The calculated
371 P-T data cluster in the range of 650-750°C and 5.5-6.5 kbar. The estimated values are in good
372 agreement with the P-T deduced for the M_3 amphibolite facies metamorphic episode recorded
373 from the enclosing felsic orthogneiss (Mukherjee et al. 2017) and the mafic dykes (Ray et al.
374 2011; Mukherjee et al. 2018b).

375 **DISCUSSIONS**

376 **Petrogenetic grid in the system CaO-MgO-Al_2O_3-SiO_2-H_2O-CO_2 and the stability of**
377 **vesuvianite + quartz**

378 In this section, topologies of the vesuvianite-bearing reactions are calculated and
379 discussed quantitatively in P-T and isobaric T-X_{CO2} fields. The simple six component system
380 CaO-MgO-Al_2O_3-SiO_2-H_2O-CO_2 (CMASV) have nine phases grossular (Grs), diopside (Di),
381 Mg-vesuvianite (Ves), anorthite (An), calcite (Cal), quartz (Qtz), wollastonite (Wo), zoisite (Zo)
382 and vapor (H_2O-CO_2). The stoichiometric composition of Mg-vesuvianite is considered to be
383 $Ca_{19}Mg_2Al_{11}Si_{18}O_{69}(OH)_9$ (Valley et al. 1985; Holland and Powell 1998). Vesuvianite and
384 clinopyroxene are considered as the only sink of Mg (see Hochella et al. 1982; Valley et al.
385 1985). In the next step, the effects of non-CMASV components (e.g. $Fe^{2+, 3+}$, F in vesuvianite,
386 $Fe^{2+, 3+}$ in clinopyroxene and garnet, Na in plagioclase) will be discussed. To develop the
387 CMASV topology, we have used the computer program PERPLE_X (version 6.7.6, updated

388 march 2017, Connolly, 2005) with the thermodynamic data base of Holland and Powell (1998,
389 revised 2002). The chemography of the chosen CMASV phases has been presented in Fig. 5.

390 **Topology in the P-T space**

391 Considering the fact that the vapor phase in the system CMASV has wide range of
392 composition, the P-T topology has been constructed for a range of X_{CO2} (molar CO_2/CO_2+H_2O)
393 values. However for each diagram, X_{CO2} remains fixed and hence the number of system
394 components becomes five. In a five-component system with nine phases, each of the non-
395 degenerate invariant point (theoretically a total of 36 non-degenerate invariant points are possible
396 in the studied system) should contain seven phases with two phases being absent in each of the
397 invariant points. However, the actual number of invariant points in the CMASV is less than 36
398 because of degeneracies arising out of the following points.

399 a) The compositions of zoisite, anorthite and calcite fall on a line (Fig. 5).
400 b) Vesuvianite and diopside are the only two Mg-bearing phases. In an invariant point, if
401 one of the two phases disappears, the other one will also disappear.

402 Fig. 6a-f shows the P-T topology of the CMASV system calculated at different X_{CO2} conditions.
403 A P-T range of 2-12 kbar and 300-900°C have been chosen as natural vesuvianite–bearing
404 assemblages in regional metamorphic belt and contact aureoles are not reported outside this
405 temperature range. Following inferences can be drawn from the P-T topologies:

406 a) Within the chosen P-T window, only two invariant points namely, [An Wo] and [An Zo]
407 are stable at very low X_{CO2} [X_{CO2}= 0.001] and at ~9 kbar. These two invariant points
408 tightly bracket the thermal stability of vesuvianite + quartz within a narrow temperature
409 range of ~300°-480°C (Fig. 6a). The thermal stability of vesuvianite + quartz does not
410 change significantly over a pressure range of 2-9 kbar.

411 b) A marginal increase in X_{CO2} (from 0.001 to 0.004), has a dramatic effect and the two
412 invariant points [An Wo] and [An Zo] shift down to a pressure close to 4 kbar (Fig. 6b).
413 Beyond X_{CO2} ~0.05, vesuvianite + quartz is no longer a stable assemblage and
414 vesuvianite alone has restricted occurrence (Fig. 6c). At X_{CO2}>0.2, vesuvianite is not
415 stable within the chosen P-T field (Fig. 6f). This observation explains why the
416 vesuvianite + quartz bearing assemblages occur at low pressure and at H_2O-rich fluid
417 compositions (Hochella et al. 1982; Valley et al. 1985; Bogoch et al. 1997).
418 c) The restricted temperature range (300-470°C) of vesuvianite + quartz even at very low
419 X_{CO2} explains why the assemblage is rare in nature though its precursor mineral
420 assemblages are preponderant in natural calc-silicate rocks over a range of P-T-fluid
421 regimes.

422 **Topology in the isobaric T-X_{CO2} space**

423 Several isobaric T-X_{CO2} topologies have been proposed for vesuvianite–bearing
424 assemblages. Trommsdorff (1968) proposed a petrogenetic grid involving vesuvianite in the
425 system CMASV based on observations of natural paragenesis. Combining the topology of
426 Trommsdorff (1968) and experimental data in the system CASV (Holdaway 1966; Greenwood
427 1967; Kerrick 1970), Kerrick et al. (1973) constructed two possible isobaric T-X_{CO2} topologies
428 involving the phases Ves-Grs-Di-Zo-Wo-An-Cal-Qtz-V. These two topologies of Kerrick et al.
429 (1973) in the CMASV system will be henceforth referred to as Top-I (Fig. 10b in Kerrick et al.
430 1973; Fig. 7a in this study) and Top-II (Fig.10a in Kerrick et al. 1973; Fig. 7b in this study). In a
431 multicomponent system, the phase rule determines the number of stable invariant points. The
432 number is highest for a non-degenerate multi-system. The topological constraints that are
433 imposed by the slopes of the univariant reactions do not allow all the possible invariant points to

be stable together (reviewed in Robinson 1991; Sengupta and Raith 2002; Groppo et al. 2013). Rather, the total number of possible invariant points (dictated by the Phase Rule) are divided into two or more clusters, each stable under a given range of intensive variables that are acting upon the chosen system (reviewed in Hensen 1986; Robinson 1991; Sengupta and Raith 2002; Groppo et al. 2013). Once critical value(s) of the intensive parameters are crossed, one cluster of invariant points changes to another cluster. This phenomenon is known as 'topological inversion' and the topologies thus related are termed as 'alternate topology' with respect to one another (Hensen 1986; Robinson 1991; Sengupta and Raith 2002). It is shown in Fig. 7 that geometrically Top-II is the alternate form of Top-I and the point of inversion occurs at point 'O' (Fig. 7). The characteristic invariant points and the univariant reactions of these two alternate topologies are presented in Table 4. Hochella et al. (1982) was the first to experimentally determine the reaction Grs + Di + Wo= Ves + Qtz in T-X_{CO2} diagram at 2 kbar. Combining their experimental data in the system CMASV and other experimentally derived CASV reactions, Hochella et al. (1982) presented a T-X_{CO2} topology that is similar to the one proposed by Trommsdorff (1968) around the invariant point [An Zo] (Fig. 8a). Using the experimental data of Hochella et al. (1982) and their own work on the stoichiometry of vesuvianite, Valley et al. (1985) proposed an exhaustive T-X_{CO2} topology that is similar to the Top-I presented by Kerrick et al.1973 (Fig. 8a).

It is to be noted that barring two cases (Hover Granath et al. 1983; Cartwright and Oliver 1994) where the natural vesuvianite-bearing assemblages and reactions support only the Top-II, all the reported vesuvianite-bearing assemblages and reactions can be explained by both Top-I and Top-II (Supplemental table 3). For this reason, many vesuvianite bearing assemblages and reactions that are not typical for either of the two topologies of Kerrick et al. (1973), are

457 arbitrarily explained in either Top-I (Rice 1983; Johnson et al. 2000; Nabelek and Morgan 2012)
458 or Top II (Labotka et al. 1988; Bogoch et al. 1997).

459 Against this backdrop we have computed the quantitative T-X_{CO2} diagram (at 2 kbar) for
460 the CMASV system over the temperature range of 300-800°C and X_{CO2} = 0-0.3. Under the given
461 P-T-X_{CO2} conditions, five invariant points [An Wo], [An Zo], [Di Wo Ves], [Qtz Wo] and [Di Zo
462 Ves] become stable (Fig. 8b). The computed topology at 2 kbar (Fig. 8b) resembles the
463 qualitative Top-I computed by Kerrick et al.(1973) and Valley et al (1985) (Fig. 8a). Fig. 8b also
464 shows the stability field of the vesuvianite-bearing assemblage vis-à-vis stability fields of other
465 commonly occurring calc-silicate assemblages (wollastonite-, zoisite-, grossular-bearing
466 assemblages) found in nature. This T-X_{CO2} topology supports the observations from P-T
467 topologies (Fig. 6) that vesuvianite bearing assemblages are stable at low X_{CO2} condition with
468 vesuvianite + quartz occurring in extremely low X_{CO2} (<0.01).

469 To show the effect of pressure, the T-X_{CO2} topologies in the CMASV system are also
470 computed at 4, 6, and 8 kbar (Fig. 8c-e). With increasing pressure, the positions of the three
471 invariant points [Qtz Wo], [Di Ves Wo] and [Di Ves Zo] change so that the stability field of
472 wollastonite- and vesuvianite-bearing assemblage shrinks but that of the zoisite-bearing
473 assemblages expand (Fig. 8c-e). The stability of vesuvianite + quartz, however, remains almost
474 insensitive to pressure change as the T-X_{CO2} coordinates of [An Wo] and [An Zo] remain
475 virtually constant with changing P (Fig. 8b-e). This observation is consistent with the P-T
476 topologies that show no significant shift in the thermal stability of vesuvianite + quartz with
477 X_{CO2} (Fig. 6a-b).

478 **Effects of non-CMASV components and inversion of the isobaric T-X_{CO2} topology**

In natural rocks, significant concentrations of non-CMASV components are recorded in vesuvianite (Na, REE^{3+}, Bi^{3+}, Pb^{2+}, Th^{4+}, Sb^{3+}, Fe^{3+},Fe^{2+},Ti^{4+}, Cr^{3+}, Mn, Cu, Zn, B, F, Cl, S; Groat et al. 1992a, 1992b), grossular (Fe^{3+}, Fe^{2+}, Mn), diopside (Fe^{3+}, Fe^{2+}, Mn, Al), anorthite (Na) and fluid (F, Cl, B, S etc.). Introduction of these non-CMASV components expands the stability field of the minerals that accommodate these elements. Consequently, the variance of the CMASV assemblages are increased through translation of the invariant points with the related univariant reactions along specific univariant lines on which the effects of the added non-CMASV components are absent (Hensen and Harley 1990; Harley and Buick 1992). As an example, if vesuvianite is the only F-bearing phase, then on addition of F to the system, all the vesuvianite-present invariant points move along their respective vesuvianite-absent reaction lines (yellow arrow in Fig. 9a) and subsequently increase the stability field of vesuvianite-bearing assemblages. Fig. 9a presents the isobaric T-X_{CO2} topology in the system CMASV where the displacement of the different CMASV invariant points due to the reduced activities of vesuvianite, grossular, diopside and anorthite are shown. The reduced activities account for the presence of non-CMASV components in end member mineral compositions of CMASV phases. Compared to the CMASV topology with end member mineral phases, the reduced activities of anorthite and vesuvianite enlarge the stability field of vesuvianite (through the translation of the invariant points along red and yellow arrow respectively shown in Fig. 9a and Fig. 9b-c). An opposite effect results for reduced activities of grossular and diopside (i.e. movement of invariant points along pink and blue arrow respectively in Fig. 9a). Net displacement of the CMASV invariant points (and the related univariant reactions) will be determined by the changes of equilibrium constant of a given univariant reaction owing to chemical substitution (Ganguly and Saxena 1987; Spear 1993). Compositions of minerals in natural vesuvianite-bearing rocks show

that, compared to other phases, vesuvianite incorporates a larger number of non-CMASV components in its cation and anion sites (Fe^{+2} Mg_{-1}, $CuMg_{-1}$, $ZnMg_{-1}$, $MnMg_{-1}$, $Fe^{+3}Al_{-1}$, $F(OH)_{-1}$, $MgTiAl_{-2}$, $Mg(OH)(AlO)_{-1}$, $TiO(AlOH)_{-1}$, $BMg(H_2Al)_{-1}$, $BMg_2(HAl_2)_{-1}$, $BAl(H_2Si)_{-1}$, $NaTi(CaAl)_{-1}$, $NaAl(CaMg)_{-1}$;Groat et al. 1992a). This and the complex stoichiometry of vesuvianite eventually control the equilibrium constant of the vesuvianite bearing reactions. The isobaric T-X_{CO2} topology is calculated with decreasing activities of vesuvianite (a_{Ves}). Fig. 10a shows how the change in a_{Ves} causes the vesuvianite-bearing CMASV invariant points and corresponding univariant reactions to slide along the vesuvianite absent lines. This effect significantly enlarges the stability field of vesuvianite + quartz bearing assemblages (bounded by reactions 1, 7, 8 and marked by darker shade; first two diagrams from left in Fig. 10a). At some specific value of a_{Ves}, the stability field of of vesuvianite + quartz enlarges up to the vesuvianite absent invariant point [Di Wo Ves]. If the a_{Ves} decreases below this specific value a topological inversion occurs (between a_{Ves} 0.1 to 0.07; compare second and third figure from left in Fig.10a). A number of invariant points which were stable at higher a_{Ves} become metastable at a_{Ves} lower than this specific value (Fig.10b). This vesuvianite activity (or equilibrium constant, if all the other phases are considered) determines the position of 'O' in Fig. 7. This inverted topology is the same as Top-II which was developed by Kerrick et al. (1973) (compare Fig.7 and Fig.10b). It is to be noted that in Top-II, vesuvianite + quartz has a larger stability field compared to Top-I at any pressure. Similar activity dependent topological inversions have been reported from many natural systems having diverse lithologies (Hensen and Harley 1990; Sengupta et al. 1991; Harley and Buick 1992; Sengupta and Raith 2002; Groppo et al. 2013). Our study, therefore, validates the isobaric T-X_{CO2} topology proposed by Valley et al. (1985) (Top-I) as well as the

524 contrasting topology (Top-II) proposed by Kerrick et al. (1973) and links these two as alternate
525 topologies.

526 **Application of the studied assemblages in the quantitative isobaric T-X_{CO2} topology**

527 The vesuvianite-garnet bearing assemblages of the studied vein can now be explained in
528 the isobaric T-X_{CO2} diagram. To delineate the T-X_{CO2} range for the studied assemblages
529 following points are considered:

530 a) The veins are devoid of zoisite and wollastonite. Therefore the T-X_{CO2} window of the
531 studied rocks must not overlap with the stability field of zoisite/wollastonite bearing
532 assemblage.
533 b) Occurrence of the critical mineral assemblage vesuvianite + quartz + calcite + anorthite
534 and textural evidence (reaction ii) supporting the characteristic reaction Di + Qtz + Cal
535 +An = Ves (Table 4) suggest that Top-II should be applicable for the studied rocks.
536 c) During calculation, the pressure was fixed at 6 kbar which is the mean pressure
537 constrained for the development of vesuvianite-garnet vein by the geothermobarometric
538 calculations.
539 d) A temperature range of 300°-900°C (the thermal stability of the high temperature
540 (>300°C)- less ordered-high symmetry vesuvianite (Allen and Burnham 1992; Elmi
541 et al. 2011)) and X_{CO2}=0.00–0.30 have been chosen as vesuvianite ± quartz occurs only
542 at low X_{CO2} (<0.3, Fig. 6, 8).
543 e) The isobaric T-X_{CO2} diagram has been calculated for measured activities of the solid
544 solution phases. The activities of grossular, diopside and anorthite have been computed
545 from their measured compositions using the a-X program
546 (https://www.esc.cam.ac.uk/research/research-groups/research-projects/tim-hollands-

547 software-pages/ax). It has been shown that the geometry of the topology in parts of the
548 system CMASV (relevant to this study) is, among other factors, strongly dependent upon
549 the a_{Ves}. In view of very low value for computed a_{Ves}, we have used an optimum activity
550 which is required to stabilize the geometry of Top-II.

551 With the aforestated constraints, the quantitative T-X_{CO2} diagram (Fig. 11) is calculated for
552 the studied vesuvianite-garnet veins. The reaction textures and the topological constraints of Fig.
553 11 suggest that an influx of H_2O- (and F-) rich fluid into the host calc-silicate rock with or
554 without temperature change could explain the formation of the vesuvianite-garnet-bearing
555 assemblage. Two T-X_{CO2} paths namely A and B are identified (Fig. 11a). Paths A and B cut the
556 univariant reactions that are located on the higher and lower temperature sides of the isobaric
557 invariant point [Wo Zo] (Fig. 11a). Path A explains the formation of vesuvianite from garnet in
558 quartz-free domains through reaction (Wo, Zo, Qtz) (reaction i from textural observations;
559 reaction 16 in Fig. 11a). Path B, on the other hand, explains the formation of vesuvianite through
560 reaction (Wo, Zo, Grs) (reaction ii from textural observations; reaction 18 in Fig. 11a) followed
561 by the formation of coronal garnet (reaction iii from textural observations; reaction 15 in Fig.
562 11a). The topological relations of Fig. 11a place constraints on the vesuvianite-garnet vein
563 formation occurred in a narrow region of temperature (620°-780°C) and fluid compositions
564 (X_{CO2}= 0.13-0.4). The inferred temperature range corroborates the temperature estimated from
565 plagioclase-amphibole thermometry.

566 Occurrence of the two near isobaric T-X_{CO2} paths (A and B; Fig. 11a) in closely spaced
567 domains (within one thin section) warrant an explanation. One plausible mechanism that can
568 explain this apparent paradox is depicted in Fig. 11b-d. In view of the presence of F-vesuvianite,
569 F-apatite and F-titanite in the vesuvianite-garnet veins, it can be presumed that the infiltrating

aqueous fluid also contained appreciable F. Fig. 11b shows that initially the infiltrating fluid was poorer in F. Vesuvianite being the major phase that accommodates F in its structure, a reduced F activity in the fluid should cause the stability field of vesuvianite-bearing assemblage (Ves + An + Cal + Qtz) to shrink. This is achieved by down temperature shift of the isobaric invariant point [Wo Zo] along the vesuvianite-free reaction 15 (Fig. 11b). Consequently, the T-X_{CO2} path of the studied rock would cut the isobaric univariant reaction line 16 and thus explain the inclusion of garnet within vesuvianite. The next pulse of the infiltrated fluid was F-rich. Consequently, the isobaric invariant point [Wo Zo] slid to higher temperature along the vesuvianite free reaction 15 resulting in an increase in the stability field of the vesuvianite-bearing assemblage Ves + An + Cal + Qtz (Fig. 11c-d). This allows the T-X_{CO2} path to cut the reaction 18 and reaction 15 successively (Fig. 11d). Operation of reaction 18 and 15 explains the formation of vesuvianite followed by formation of the coronal garnet. Even a small shift of the isobaric invariant point [Wo Zo], presumably due to the variation in the F-content of the infiltrating fluid, may stabilize these two assemblages if the temperature of equilibration remains close to $T_{[Wo\ Zo]}$, which is the case here (Fig.11c).

The source of H_2O + F rich fluid that was instrumental for development of vesuvianite in the studied vein cannot be traced with certainty. However, several features point to a genetic relation between the quartzo-feldspathic pegmatitic and the vesuvianite-garnet-bearing veins: (a) both the veins occur in close proximity to each other, (b) both cut the fabric of the host calc-silicate rocks, and (c) similar to the minerals in the pegmatitic veins, the vesuvianite and garnet grains too do not show any evidence of deformation. It is therefore presumed that the crystallization of pegmatites could have provided the H_2O + F fluid that permeated into the host calc-silicate rock and produced vesuvianite-garnet-rich veins. Presence of ferric ion within vesuvianite and garnet

593 indicates that the infiltrating fluid was oxidizing. Preferential development of vesuvianite (in
594 plagioclase-rich layer) and garnet (in clinopyroxene-rich layer) and uniform composition of these
595 two minerals in both the domains suggests controls of local bulk compositions combined with
596 fluid composition.

597 **IMPLICATIONS**

598 Mineral assemblages that develop in a given natural system at a specific (or in a range of)
599 P-T-X conditions are primarily dictated by the reaction geometry in the multicomponent system.
600 In some multicomponent systems, the slopes of the univariant reactions around the related
601 invariant points are such that there can be more than one reaction topology at a given P-T-fluid
602 composition (Hensen 1986; Hensen and Harley 1990; Harley and Buick 1992; Sengupta and
603 Raith 2002). In this study we have demonstrated the phenomenon and controls of topological
604 inversion in parts of the system CMASH with vesuvianite- bearing assemblages and discussed its
605 consequences. Our study stresses the need to choose appropriate reaction topology in order to
606 avoid wrong interpretation about the stability (or instability) of a given mineral assemblages in
607 the complex natural rocks.

608 **ACKNOWLEDGEMENTS**

609 A.D. acknowledges financial support from the Council of Scientific and Industrial
610 Research (CSIR), New Delhi. SRC acknowledges financial support from Department of Atomic
611 Energy, India and The Board of Research in Nuclear Sciences (DAE-BRNS). S.M.
612 acknowledges financial support from the University Grants Commission (UGC), New Delhi.
613 P.S. and S.S. acknowledge the grants received from the following programs awarded to the
614 Department of Geological Sciences, Jadavpur University: University Potential for Excellence
615 (UPE-Phase II) from UGC, Promotion of University Research and Scientific Excellence from

DST (Department of Science and Technology, India), Fund for Improvement of Science and Technology (FIST-Phase II) from DST and Center of Advance Studies (CAS-phase VI) from UGC. We thank Dr. Chiara Groppo, an anonymous reviewer and the associate editor Dr. Callum Hetherington for their inspiring and constructive reviews. We also thank the editor and the associate editor for their efficient editorial handling.

REFERENCES

Acharyya, S.K. (2003) The Nature of Mesoproterozoic Central Indian Tectonic Zone with Exhumed and Reworked Older Granulites. Gondwana Research, 6, 197–214.

Ahmed-Said, Y., and Leake, B.E. (1996) The conditions of metamorphism of a grossular-wollastonite vesuvianite skarn from the Omey Granite, Connemara, western Ireland, with special reference to the chemistry of vesuvianite. Mineralogical Magazine, 60, 541–550.

Allen, F.M., and Burnham, C.W. (1992) A comprehensive structure-model for vesuvianite; symmetry variations and crystal growth. The Canadian Mineralogist, 30, 1–18.

Anderson, J.L., and Smith, D.R. (1995) The effects of temperature and fo2 on the Al-in-hornblende barometer. American Mineralogist, 80, 549–559.

Arem, J.E. (1973) Idocrase (vesuvianite)—A 250-year puzzle. Mineralogical Record, 4, 164–174.

Armbruster, T., and Edwin, G. (2000a) P4/n and P4nc long-range ordering in low-temperature vesuvianites. American Mineralogist.

——— (2000b) Tetrahedral vacancies and cation ordering in low-temperature Mn-bearing vesuvianites: Indication of a hydrogarnet-like substitution. American Mineralogist.

Balassone, G., Talla, D., Beran, A., Mormone, A., Altomare, A., Moliterni, A., Mondillo, N.,

638 Saviano, M., and Petti, C. (2011) Vesuvianite from Somma-Vesuvius volcano (southern
639 Italy): Chemical, X-ray diffraction and single-crystal polarized FTIR investigations.
640 Periodico di Mineralogia Vol. 80.

641 Bhattacharya, B.P. (1976) Metamorphism of the Precambrian rocks of the central part of Santhal
642 Parganas district, Bihar. Quarternary Journal of the Geology, Mining and Metallurgical
643 Society of India, 48, 183–196.

644 Bogoch, R.O.N., Kumarapeli, S., and Matthews, A. (1997) High-Pressure Assemblage in the
645 Central Metasedimentary Province , Belt of the Grenville Quebec, 35, 1269–1275.

646 Cartwright, I., and Oliver, N.H.S. (1994) Fluid flow during contact metamorphism at Mary
647 Kathleen, Queensland, Australia. Journal of Petrology, 35, 1493–1519.

648 Chatterjee, N. (2018) An assembly of the Indian Shield at c. 1.0 Ga and shearing at c. 876-784
649 Ma in Eastern India: insights from contrasting PT paths, and burial and exhumation rates of
650 metapelitic granulites. Precambrian Research.

651 Chatterjee, N., and Ghose, N.C. (2011) Extensive Early Neoproterozoic high-grade
652 metamorphism in North Chotanagpur Gneissic Complex of the Central Indian Tectonic
653 Zone. Gondwana Research, 20, 362–379.

654 Chatterjee, N., Crowley, J.L., and Ghose, N.C. (2008) Geochronology of the 1.55Ga Bengal
655 anorthosite and Grenvillian metamorphism in the Chotanagpur gneissic complex, eastern
656 India. Precambrian Research, 161, 303–316.

657 Chatterjee, N., Banerjee, M., Bhattacharya, A., and Maji, A.K. (2010) Monazite chronology ,
658 metamorphism – anatexis and tectonic relevance of the mid-Neoproterozoic Eastern Indian
659 Tectonic Zone. Precambrian Research, 179, 99–120.

660 Connolly, J.A.D. (2005) Computation of phase equilibria by linear programming: A tool for
661 geodynamic modeling and its application to subduction zone decarbonation.

662 Dey, A., Mukherjee, S., Sanyal, S., Ibanez-Mejia, M., and Sengupta, P. (2017) Deciphering
663 Sedimentary Provenance and Timing of Sedimentation From a Suite of Metapelites From
664 the Chotanagpur Granite Gneissic Complex, India: Implications for Proterozoic Tectonics
665 in the East-Central Part of the Indian Shield. In R. Mazumder, Ed., Sediment Provenance;
666 Influences on compositional change from source to sink pp. 453–486. Elsevier Ltd.

667 Droop, G.T.R. (1987) A General Equation for Estimating Fe3+ Concentrations in
668 Ferromagnesian Silicates and Oxides from Microprobe Analyses, Using Stoichiometric
669 Criteria. Mineralogical Magazine, 51, 431–435.

670 Ellis, D.J., and Green, D.H. (1979) An experimental study of the effect of Ca upon garnet-
671 clinopyroxene Fe-Mg exchange equilibria. Contributions to Mineralogy and Petrology, 71,
672 13–22.

673 Elmi, C., Brigatti, M.F., Pasquali, L., Montecchi, M., Laurora, A., Malferrari, D., and
674 Nannarone, S. (2011) High-temperature vesuvianite: crystal chemistry and surface
675 considerations. Physics and Chemistry of Minerals, 38, 459–468.

676 Enami, M., Suzuki, K., Liou, J., and Bird, D.K. (1993) Al-Fe3+ and F-OH substitutions in
677 titanite and constraints on their P-T dependence, 219-231 p. European Journal of
678 Mineralogy Vol. 5.

679 Franz, G., and S. Spear, F. (1985) Aluminous titanite (sphene) from the Eclogite Zone, south-
680 central Tauern Window, Austria, 33-46 p. Chemical Geology - CHEM GEOL Vol. 50.

681 Galuskin, E. V., Armbruster, T., Malsy, A., Galuskina, I.O., and Sitarz, M. (2003) Morphology,

composition and structure of low-temperature P4/nnc high-fluorine vesuvianite whiskers from Polar Yakutia, Russia. Canadian Mineralogist, 41, 843–856.

Ganguly, J., and Saxena, S.K. (1987) Mixtures and mineral reactions. Springer, Berlin Heidelberg New York.

Greenwood, H.J. (1967) Wollastonite-stability in H2O-CO2 mixtures and occurence in a contact-metamorphic aureole near Salmo British Columbia Canada. American Mineralogist, 52, 1669–+.

Grew, E.S., Locock, A.J., Mills, S.J., Galuskina, I.O., Galuskin, E. V, and Hålenius, U. (2013) Nomenclature of the garnet supergroup. American Mineralogist, 98, 785–811.

Groat, L.A., Hawthorne, F.C., and Ercit, T.S. (1992a) The chemistry of Vesuvianite. Canadian Mineralogist, 30, 19–48.

Groat, L.A., Hawthorne, F.C., and Ercit, T.S. (1992b) The role of fluorine in vesuvianite: A crystal-structure study. Canadian Mineralogist, 30, 1065.

Groat, L.A., Hawthorne, F.C., and Ercit, T.S. (1994) Excess Cations in the Crystal Structure of Vesuvianite. The Canadian Mineralogist, 32, 497–504.

Groppo, C., Rolfo, F., Castelli, D., and Connolly, J. a D. (2013) Metamorphic CO2 production from calc-silicate rocks via garnet-forming reactions in the CFAS-H2O-CO2 system. Contributions to Mineralogy and Petrology, 166, 1655–1675.

Halama, R., Savov, I.P., Garbe-Schönberg, D., Schenk, V., and Toulkeridis, T. (2013) Vesuvianite in high-pressure-metamorphosed oceanic lithosphere (Raspas Complex, Ecuador) and its role for transport of water and trace elements in subduction zones. European Journal of Mineralogy, 25, 193–219.

704 Harley, S.L., and Buick, I.S. (1992) Wollastonite—Scapolite Assemblages as Indicators of
705 Granulite Pressure-Temperature-Fluid Histories: The Rauer Group, East Antarctica. Journal
706 of Petrology, 33, 693–728.

707 Hensen, B.J. (1986) Theoretical phase relations involving cordierite and garnet revisited: the
708 influence of oxygen fugacity on the stability of sapphirine and spinel in the system Mg-Fe-
709 Al-Si-O. Contributions to Mineralogy and Petrology, 92, 362–367.

710 Hensen, B.J., and Harley, S.L. (1990) Graphical analysis of P—T—X relations in granulite
711 facies metapelites. In High-temperature metamorphism and crustal anatexis pp. 19–56.
712 Springer.

713 Hochella, M.F., Liou, J.G., Keskinen, M.J., and Kim, H.S. (1982) Synthesis and Stability
714 Relations of Magnesium Idocrase. Economic geology, 77, 798–808.

715 Hoisch, T.D. (1985) The solid solution chemistry of vesuvianite. Contributions Mineralogy
716 Petrology, 89, 205–214.

717 Holdaway, M.J. (1966) Hydrothermal stability of clinozoisite plus quartz. American Journal of
718 Science, 264, 643–667.

719 Holland, T., and Blundy, J. (1994) Non-ideal interactions in calcic amphiboles and their bearing
720 on amphibole-plagioclase thermometry. Contributions to Mineralogy and Petrology, 116,
721 433–447.

722 Holland, T.J.B., and Powell, R. (1998) An internally consistent thermodynamic data set for
723 phases of petrological interest. Journal of Metamorphic Geology, 16, 309–343.

724 Hover Granath, V.C., Papike, J.J., and Labotka, T.C. (1983) The Notch Peak Contact
725 Metamorphic Aureole , Utah : Petrology of the Big Horse Limestone Member of the Orr

726 Formation. Geological Society of America Bulletin, 94, 889–906.

727 Johnson, T.E., Hudson, N.F.C., and Droop, G.T.R. (2000) Wollastonite-bearing assemblages
728 from the Dalradian at Fraserburgh , northeast Scotland and their bearing on the
729 emplacement of garnetiferous granitoid sheets. Mineralogical Magazine, 64, 1165–1176.

730 Karmakar, S., Bose, S., Sarbadhikari, A.B., and Das, K. (2011) Evolution of granulite enclaves
731 and associated gneisses from Purulia, Chhotanagpur Granite Gneiss Complex, India:
732 Evidence for 990-940Ma tectonothermal event(s) at the eastern India cratonic fringe zone.
733 Journal of Asian Earth Sciences, 41, 69–88.

734 Kerrick, D.M. (1970) Contact metamorphism in some areas of the Sierra Nevada, California.
735 Geological Society of America Bulletin, 81, 2913–2938.

736 Kerrick, D.M., Crawford, K.E., and Randazzo, A.F. (1973) Metamorphism of calcareous rocks
737 in three roof pendants in the Sierra Nevada, California. Journal of Petrology, 14, 303–325.

738 Ketcham, R.A. (2015) Calculation of stoichiometry from EMP data for apatite and other phases
739 with mixing on monovalent anion sites. American Mineralogist, 100, 1620–1623.

740 Kretz, R. (1983) Symbols for rock-forming minerals. American Mineralogist, 68, 277–279.

741 Labotka, T.C., Nabelek, P.I., and Papike, J.J. (1988) Fluid infiltration through the Big Horse
742 Limestone Member in the Notch Peak contact-metamorphic aureole, Utah. American
743 Mineralogist, 73, 1302–1324.

744 Leake, B.E., Woolley, A.R., Arps, C.E.S., Birch, W.D., Gilbert, M.C., Grice, J.D., Hawthorne,
745 F.C., Kato, A., Kisch, H.J., and Krivovichev, V.G. (1997) Report. Nomenclature of
746 amphiboles: report of the subcommittee on amphiboles of the international mineralogical
747 association commission on new minerals and mineral names. Mineralogical magazine, 61,

748 295–321.

749 Leake, B.E., Woolley, A.R., Birch, W.D., Burke, E.A.J., Ferraris, G., Grice, J.D., Hawthorne,
750 F.C., Kisch, H.J., Krivovichev, V.G., Schumacher, J.C., and others (2004) Nomenclature of
751 amphiboles: Additions and revisions to the International Mineralogical Association's
752 amphibole nomenclature. American Mineralogist, 89, 883–887.

753 Maji, A.K., Goon, S., Bhattacharya, A., Mishra, B., Mahato, S., and Bernhardt, H. (2008)
754 Proterozoic polyphase metamorphism in the Chhotanagpur Gneissic Complex (India), and
755 implication for trans-continental Gondwanaland correlation. Precambrian Research, 162,
756 385–402.

757 Markl, G., and Piazolo, S. (1999) Stability of high-Al titanite from low-pressure calcsilicates in
758 light of fluid and host-rock composition. American Mineralogist.

759 Mukherjee, S., Dey, A., Sanyal, S., Ibanez-Mejia, M., Dutta, U., and Sengupta, P. (2017)
760 Petrology and U–Pb geochronology of zircon in a suite of charnockitic gneisses from parts
761 of the Chotanagpur Granite Gneiss Complex (CGGC): evidence for the reworking of a
762 Mesoproterozoic basement during the formation of the Rodinia supercontinent. Geological
763 Society, London, Special Publications, 457, SP457-6.

764 Mukherjee, S., Dey, A., Ibanez-Mejia, M., Sanyal, S., and Sengupta, P. (2018a) Geochemistry,
765 U-Pb geochronology and Lu-Hf isotope systematics of a suite of ferroan (A-type) granitoids
766 from the CGGC: Evidence for Mesoproterozoic crustal extension in the east Indian shield.
767 Precambrian Research, 305, 40–63.

768 Mukherjee, S., Dey, A., Sanyal, S., and Sengupta, P. (2018b) Tectonothermal imprints in a suite
769 of mafic dykes from the Chotanagpur Granite Gneissic complex (CGGC), Jharkhand, India:

770 Evidence for late Tonian reworking of an early Tonian continental crust. Lithos, 320–321,
771 490–514.

772 ——— (2019) Proterozoic Crustal Evolution of the Chotanagpur Granite Gneissic Complex,
773 Jharkhand-Bihar-West Bengal, India: Current Status and Future Prospect. In S. Mukherjee,
774 Ed., Tectonics and Structural Geology: Indian Context pp. 7–54. Springer, Cham.

775 Nabelek, P.I., and Morgan, S.S. (2012) Metamorphism and fluid flow in the contact aureole of
776 the Eureka Valley–Joshua Flat–Beer Creek pluton, California. Bulletin, 124, 228–239.

777 Nabelek, P.I., Bédard, J.H., Hryciuk, M., and Hayes, B. (2013) Short-duration contact
778 metamorphism of calcareous sedimentary rocks by Neoproterozoic Franklin gabbro sills
779 and dykes on Victoria Island, Canada. Journal of Metamorphic Geology, 31, 205–220.

780 Ogorodova, L.P., Kiseleva, I.A., Melchakova, L. V, and Spiridonov, E.M. (2011)
781 Thermodynamic characteristics of minerals of the vesuvianite group. Geochemistry
782 International, 49, 191–195.

783 Palache, C. (1935) The minerals of Franklin and Sterling Hill, Sussex County, New Jersey. US
784 Government Printing Office.

785 Panikorovskii, L.T., Chukanov, V.N., Rusakov, S.V., Shilovskikh, V.V., Mazur, S.A.,
786 Balassone, G., Ivanyuk, Y.G., and Krivovichev, V.S. (2017) Vesuvianite from the Somma-
787 Vesuvius Complex: New Data and Revised Formula. Minerals .

788 Patel, S.C. (2007) Vesuvianite-wollastonite-grossular-bearing calc-silicate rock near Tatapani,
789 Surguja district, Chhattisgarh. Journal of Earth System Science, 116, 143–147.

790 Ray, S., Sanyal, S., and Sengupta, P. (2011) Mineralogical Control on Rheological Inversion of a
791 Suite of Deformed Mafic Dykes from Parts of the Chottanagpur Granite Gneiss Complex of

792 Eastern India. In R.K. Srivastava, Ed., Dyke Swarms: Keys for Geodynamic Interpretation
793 pp. 263–276. Springer-Verlag Berlin Heidelberg.

794 Rekha, S., Upadhyay, D., Bhattacharya, A., Kooijman, E., Goon, S., Mahato, S., and Pant, N.C.
795 (2011) Lithostructural and chronological constraints for tectonic restoration of Proterozoic
796 accretion in the Eastern Indian Precambrian shield. Precambrian Research, 187, 313–333.

797 Rice, J.M. (1983) Metamorphism of rodingites: Part I. Phase relations in a portion of the system
798 CaO–MgO–Al2O3–SiO2–CO2–H2O. American Journal of Science, 283, 121–150.

799 Robinson, P. (1991) The eye of the petrographer, the mind of the petrologist. American
800 mineralogist, 76, 1781–1810.

801 Roy Choudhury, S., Mukherjee, S., Dey, A., Sanyal, S., and Sengupta, P. (2016) Reaction
802 textures in some calc-silicate enclaves from the Chotanagpur Granite Gneissic Complex,
803 and their implications. In XXXVII Annual meeting of the Electron microscope society of
804 India pp. 84–85.

805 Saikia, A., Gogoi, B., Kaulina, T., Lialina, L., Bayanova, T., and Ahmad, M. (2017)
806 Geochemical and U – Pb zircon age characterization of granites of the Bathani Volcano
807 Sedimentary sequence , Chotanagpur Granite Gneiss Complex , eastern India : vestiges of
808 the Nuna supercontinent in the Central Indian Tectonic Zone. Geological Society, London,
809 Special Publications, 457.

810 Sanyal, S., and Sengupta, P. (2012) Metamorphic evolution of the Chotanagpur Granite Gneiss
811 Complex of the East Indian Shield: current status. Geological Society, London, Special
812 Publications, 365, 117–145.

813 Sengupta, P., and Raith, M.M. (2002) Garnet composition as a petrogenetic indicator: An

example from a marble -calc-silicate granulite interface at kondapalle, Eastern Ghats Belt, India. American Journal of Science, 302, 686–725.

Sengupta, P., Karmakar, S., Dasgupta, S., and Fukuoka, M. (1991) Petrology of spinel granulites from Araku, Eastern Ghats, India, and a petrogenetic grid for sapphirine-free rocks in the system FMAS. Journal of Metamorphic Geology, 9, 451–459.

Sengupta, P., Sanyal, S., Dasgupta, S., Fukuoka, M., and Ehl, J. (1997) Controls of mineral reactions in high-grade garnet-wollastonite-scapolite-bearing calcsilicate rocks: an example from Anakapalle, Eastern Ghats, India. Journal of Metamorphic Geology, 15, 551–564.

Sengupta, P., Raith, M.M., and Datta, A. (2004) Stability of fluorite and titanite in a calc-silicate rock from the Vizianagaram area, Eastern Ghats Belt, India. Journal of Metamorphic Geology, 22, 345–359.

Singh, R.N., Thorpe, R., and Kristic, D. (2001) Galena Pb-isotope data of base metal occurrences in the Hesatu-Belbathan belt, eastern Precambrian shield. Jour. Geol. Soc. India, 57, 535–538.

Smith, D.C. (1981) The pressure and temperature dependence of Al-solubility in sphene in the system Ti-Al-Ca-Si-OF. Progress in Experimental Petrology NERC Publication Series, D-18, 193–197.

Spear, F.S. (1993) Metamorphic Phase Equilibria and Pressure-Temperature-Time Paths. Monograph 1, 799 p. Mineralogical Society of America.

Tracy, R.J., and Frost, B.R. (1991) Phase equilibria and thermobarometry of calcareous, ultramafic and mafic rocks, and iron formations. Reviews in Mineralogy and Geochemistry, 26, 207–289.

836 Tracy, R.J., Jaffe, H.W., and Robinson, P. (1978) Monticellite marble at Cascade Mountain.
837 Adirondack Mountains. New York. American Mineralogist, 63, 991–999.

838 Troitzsch, U., and Ellis, D.J. (2002) Thermodynamic properties and stability of AlF-bearing
839 titanite CaTiOSiO4–CaAlFSiO4. Contributions to Mineralogy and Petrology, 142, 543–
840 563.

841 Trommsdorff, V. (1968) Mineralreaktionen mit Wollastonit und Vesuvian in einem
842 Kalksilikatfels der alpinen Disthenzone (Claro , Tessin). Schweiz. miner. petrogr. Mitt.,
843 48, 655–666.

844 Valley, J.W., and Essene, E.J. (1979) Vesuvianite, akermanite, monticellite and wollastonite
845 equilibria and high XH2o/CO2 at Cascade slide, Mt Marcy Quad, Adirondack Mts. EOS,
846 60, 423.

847 Valley, J.W., Essene, E.J., and Peacor, D.R. (1983) Fluorine-bearing garnets in Adirondack calc-
848 silicates. American Mineralogist, 68, 444–448.

849 Valley, J.W., Peacor, D.R., and Essene, E.J. (1985) Crystal chemistry of a Mg-vesuvianite and
850 implications of phase equilibria in the system CaO-MgO-Al2O3-SiO2-H2O-CO2. Journal
851 of Metamorphic Geology, 3, 137–153.

852 Zanoni, D., Rebay, G., and Spalla, M. (2016) Ocean floor and subduction record in the Zermatt-
853 Saas rodingites, Valtournanche, Western Alps. Journal of Metamorphic Geology.

854 FIGURE CAPTIONS

855 **Figure 1. (a)** Geological map of the CGGC (modified after Acharyya 2003). Red square box
856 indicates the study area located in the north-eastern part of the terrane. Inset shows the location
857 of the CGGC within India. **(b)** Map showing major lithological distributions of the study area,

858 modified after the geological map of Jharkhand, 1:250000 scale, published by Geological Survey
859 of India in 2001.

860 **Figure 2. (a)** Alternate plagioclase and clinopyroxene rich layers in the host calc-silicate rock.
861 **(b)** Vesuvianite-garnet veins parallel and at low angle with respect to the gneissosity of the host
862 rock. Within the veins, garnet-rich zones grades to vesuvianite-rich zones. **(c)** Plagioclase-
863 vesuvianite rich domain of the vein. **(d)** Vesuvianite-garnet veins partially mimic the boudinage
864 structures defined by the primary clinopyroxene-rich layers. Note the extensive replacement of
865 clinopyroxene by garnet. **(e)** Ramifying quartzo-feldspathic pegmatitic veins parallel to or at low
866 angle to the foliation of the host rock. **(f)** Pegmatitic quartzo-feldspathic vein with large
867 amphibole grains scattered within them. They are bordered by distinct amphibole rich selvages.
868 **Figure 3. (a)** Clinopyroxene and plagioclase rich bands in host calc-silicate rock. **(b)**
869 Clinopyroxene and plagioclase grains in host calc-silicate rock stretched parallel to the direction
870 of foliation in host calc-silicate rock. **(c)** Amphibole replacing clinopyroxenes in host calc-
871 silicate rock. **(d)** Coarse plagioclase and quartz showing interlocking texture in the pegmatitic
872 veins; rare clinopyroxene present as relict phase. **(e)** Large amphibole grains within the
873 pegmatitic veins. **(f)** BSE image showing replacement of Pl_1 by randomly oriented micro-veins
874 and patches of Pl_2 adjacent to amphibole grains within the pegmatitic vein. **(g-h)** PPL and CPL
875 image showing different domains (A & B) and subdomains (B1 & B2) within vesuvianite-garnet
876 veins.
877 **Figure 3. continued. (i-j)** PPL and CPL image showing mutual relations between different
878 minerals in vesuvianite rich domains (domain A) of vesuvianite-garnet veins. Note vesuvianites
879 grow over a recrystallized mosaic defined by plagioclase and clinopyroxene. **(k-l)** PPl and CPL
880 images representing vesuvianite grain from domain A with inclusions of clinopyroxene,

plagioclase, garnet, titanite and apatite. Note the presence of thin coronal garnet that separates clinopyroxene and plagioclase. **(m)** Vesuvianite partially engulfing clinopyroxene and plagioclase within domain A. Quartz and titanite present as inclusions within vesuvianite. **(n)** Partially grown coronal garnet separating clinopyroxene from plagioclase in domain A. **(o-p)** PPL and CPL images of domain B1 where small subhedral garnet grains form a dense network with clinopyroxene, titanite and plagioclase and rare quartz occurring in the interstitial spaces. The formation of garnet between clinopyroxene and plagioclase should be noted. **(q)** Stumpy vesuvianite grain within the garnet framework in domain B2. Unlike its boundary with clinopyroxene and plagioclase, garnet shares straight grain boundaries with vesuvianite.

Figure 4. (a) Representative clinopyroxene compositions from the host calc-silicate rock and the vesuvianite-garnet veins plotted in pyroxene quadrilateral. **(b)** Composition of plagioclase from host calc-silicate rock, quartzo-feldspathic pegmatitic vein and vesuvianite-garnet veins plotted on albite-anorthite join. **(c)** Composition of amphiboles from the host calc-silicate rock and quartzo-feldspathic pegmatitic vein presented in a $Mg/(Mg + Fe^{+2})$ vs Si (apfu) plot for calcic amphiboles after the classification scheme of Leake et al.(2004, 1997).

Figure 5. Chemographic relations of the phases in the CaO-MgO-Al_2O_3-SiO_2 volume. CO_2+H_2O are considered excess. The phases that lie on and above the CaO- Al_2O_3-SiO_2 plane are marked with solid and hollow circles respectively.

Figure 6. a-f) P-T topology of the CMASV system calculated at different X_{CO2} conditions. The reaction numbers are consistent throughout the figures a-f. The lighter shaded region represents the stability fields of vesuvianite while the darker shaded region represents the stability field of vesuvianite-quartz assemblage. Reaction equations are written with the high T assemblage to the

right of the = sign (reaction that has changing slopes with $X_{CO2,}$ is named following the slope of its first appearance).

Figure 7. Two possible isobaric T-X_{CO2} topologies constructed by Kerrick et al. (1973) in the CMASV system involving the phases vesuvianite-grossular-diopside-zoisite-wollastonite-anorthite-calcite-quartz-vapor. **(a)** and **(b)** represent fig.10b and 10a from Kerrick et al. (1973) and are designated here as topology I and II respectively. Note the inversion of one topology to the other in 3D space across the hypothetical co-ordinates of 'O' implying Top-I and II are alternate topologies. Stable portions of univariant equilibria are shown in solid lines, metastable extensions are dashed. Metastable univariant lines that are marked with same color, intersect to produce metastable invariant points, represented by similar colored stars. Stable invariant points are shown with solid black dots. The pink lines join the respective pair of stable and metastable invariant points and depict inversion of stability across point 'O'. The numbers within circles represent the reaction numbers.

Figure 8. (a) Qualitative T-X_{CO2} diagram in CMASV(H_2O-CO_2) system involving the phases vesuvianite-grossular-diopside-zoisite-wollastonite-anorthite-calcite-quartz-vapor at constant P (≤2 kbar) modified after Valley et al. (1985). Invariant points A, B, I and II are same as in Valley et al. (1985). The dotted line (reaction 1) represents an additional reaction plotted by Kerrick et. al. (1973), not present in Valleys' grid. The dashed lines represent the parts of Valleys' grid which constitute the topology (Top-I) calculated by Kerrick et al. (1973). The lines with alternate dash and dots (reactions 7, 8) represent the experimentally determined reactions by Hochella et al. (1982). The numbers within circles represent the reaction numbers.

Figure 8. (b-e) T-X_{CO2} diagram at isobaric pressure 2, 4, 6 and 8 kbar respectively in CAMSV(H_2O- CO_2) system computed by Perple_X program using thermodynamic dataset of

Holland & Powell 1998 (updated in 2002). The inset shows zoomed in portion of the grid marked with thick dashed rectangle. The stability fields of the vesuvianite-bearing assemblage vis-à-vis stability fields of other commonly occurring calc-silicate assemblages found in nature are marked in the figure. The reaction numbers are same as in Fig. 8a.

Figure 9. (a) Schematic representation of the effect of non-CMASV components (that results in reduced activities of minerals) on the CMASV topology at an intermediate representative pressure of 5 kbar. The colored arrows indicate the sense of movement of different CMASV invariant points with decreasing activities of vesuvianite, grossular, diopside and anorthite. The reaction numbers (in circles) are same as in Fig. 8a. The grey field represents the stability field of vesuvianite-bearing assemblages. **(b-c)** Schematic representations of the gradual increase in the stability fields of vesuvianite-bearing assemblages (marked with gradual darker shades of grey) in response to decreasing activity of anorthite (Fig. 9b) and vesuvianite (Fig. 9c).

Figure 10. (a) Isobaric T-X_{CO2} diagrams calculated in CMASV system at 5 kbar with decreasing activity of vesuvianite (a_{Ves}=0.5, 0.1, 0.07 and 0.05 respectively). The CMASV invariant points and univariant reactions slide with decreasing a_{Ves}. At some specific value of vesuvianite activity (in between a_{Ves}=0.1 and 0.07), the stability of vesuvianite + quartz enlarges upto [Di Wo Ves] invariant point and a topological inversion occurs where [An Wo], [Qtz Wo] and [Cal Wo] become unstable and [Wo Zo] and [Grs Wo] gain stability. The portions of petrogenetic grid with multiple invariant points (box i, ii and iii) are blown up for clarity.

Figure 10. (b) Enlarged image of box i and box ii from Fig.10a showing the inversion of one topology to the other across the co-ordinates of 'O' in three dimensional T-X_{CO2}-a_{Ves} space. The metastable portions of univariant reaction lines in T-X_{CO2} plane are shown with colored dashed lines and the reactions are named in corresponding colors. The metastable lines intersect at

949 metastable invariant points (marked with solid colored circles). The stable invariant points are
950 marked with solid black circles. Note change in topology of T-X_{CO2} sections as a function of
951 a_{Ves}. The pink lines join the respective pair of stable and metastable invariant points and depict
952 inversion of stability across point 'O'.

953 **Figure 11. (a)** The quantitative T-X_{CO2} diagram constructed at 6 kbar with corrected activities of
954 the solid solution phases (a_{Grs}=0.43, a_{An}=0.96, a_{Di}=0.56, a_{Ves}=0.1e^{-3}). The reaction numbers are
955 same as Fig. 10a. Path A and B explains the formation of vesuvianite and coronal garnet
956 respectively through reactions (marked by blue and red lines) as seen in the studied rocks. The
957 pink arrows show the direction of movement of the invariant points with decreasing a_{Ves}. **(b-d)**
958 Shifting of invariant points and corresponding changes in the stability fields of mineral
959 assemblages with reducing a_{Ves} (as a result of increasing F activity in infiltrating fluid). Note
960 with reducing a_{Ves}, the same T-X_{CO2} path (marked with yellow arrow) can cut different reaction
961 lines to produce different reaction textures involving vesuvianite and garnet as seen in the
962 studied rock.

This is a preprint, the final version is subject to change, of the American Mineralogist (MSA)
Cite as Authors (Year) Title. American Mineralogist, in press.
DOI: https://doi.org/10.2138/am-2019-6811

963

TABLES

Table 1. Representative compositional analyses of clinopyroxene and amphibole from host calc-silicate rock, quartzo-feldspathic pegmatitic vein and vesuvianite-garnet veins from the CGGC (stoichiometry of pyroxene is calculated on the basis of 6 oxygens; stoichiometry of amphibole is calculated after Leake et. al. 1997, 2004).

Mineral	Clinopyroxene							
Rocktype	Host calc-silicate gneiss (AS32H1)		Vesuvianite-garnet vein (D4)					
Point no.	1 / 1.	12 / 1.	9 / 1.	1/ 33.	50 / 1.	46 / 1.	24 / 1.	62 / 1.
texture			Domain A		Domain B		Inclusions in ves (Domain A & B2)	
SiO_2	52.03	52.64	51.33	50.11	51.77	52.2	51.44	51.74
TiO_2	0.09	0.08	0.14	0.1	0.1	0.09	0.1	0.16
Al_2O_3	1.27	1.27	1.9	1.79	1.88	1.77	2.14	2.13
Cr_2O_3	0.14	0.19	0.01	0.01	0.09	0.01	0	0.03
FeO	12.78	11.87	13.7	13.74	13.56	12.89	12.57	12.78
MnO	0.26	0.37	0.38	0.37	0.32	0.49	0.41	0.46
MgO	9.91	10.78	8.95	9.13	9.16	9.23	9.02	8.9
CaO	23.73	24.22	23.79	23.99	23.4	23.32	23.25	23.12
Na_2O	0.25	0.23	0.25	0.2	0.22	0.24	0.27	0.19
K_2O	0.01	0.02	0	0.01	0.02	0.01	0.05	0.01
Total	100.47	101.67	100.5	99.45	100.52	100.25	99.25	99.52
Si	1.98	1.97	1.96	1.93	1.97	1.99	1.98	1.99
Ti	0	0	0	0	0	0	0	0
Al	0.06	0.06	0.09	0.08	0.08	0.08	0.1	0.1
Cr	0	0.01	0	0	0	0	0	0
Fe^{+3}	0	0.02	0.01	0.07	0	0	0	0
Fe^{+2}	0.41	0.35	0.43	0.38	0.43	0.41	0.4	0.41
Mn	0.01	0.01	0.01	0.01	0.01	0.02	0.01	0.02
Mg	0.56	0.6	0.51	0.52	0.52	0.53	0.52	0.51
Ca	0.97	0.97	0.97	0.99	0.96	0.95	0.96	0.95
Na	0.02	0.02	0.02	0.01	0.02	0.02	0.02	0.01
K	0	0	0	0	0	0	0	0
Sum	4	4	4	4	4	4	4	4
Agt	0	0.01	0	0.01	0	0	0	0
Jd	0.01	0	0.01	0	0.02	0.04	0.03	0.05
AlTs	0.01	0.01	0.02	0.01	0.01	0	0.01	0
Don	0	0.01	0.01	0.01	0.01	0.01	0.01	0.01
X_{Mg}	0.58	0.63	0.54	0.58	0.55	0.56	0.56	0.55

Amphibole						
Rocktype	Host calc-silicate gneiss (AS32H1)		Quartzo-feldspathic pegmatitic vein (AS32Diii)			
Point no.	11 / 1.	13 / 1.	2 / 1.	22 / 1.	23 / 1.	44 / 1.
SiO_2	42.37	44.65	42.34	42.93	42.6	43.01
TiO_2	0.5	0.68	0.92	1.05	1.34	1.43
Al_2O_3	12.68	10.02	11.08	10.45	10.63	10.81
Cr_2O_3	1.35	1.48	0.13	0.09	0.1	0.2
FeO	14.73	14.63	17.63	18.1	18.57	20.09
MnO	0.29	0.27	0.3	0.03	0.31	0.21
MgO	9.48	11.05	9.6	9.6	8.92	8.76
CaO	12.24	12.29	12.1	12.01	11.86	12.33
Na_2O	1.18	0.97	1.24	1.17	1.02	1.09
K_2O	2.24	1.84	1.77	1.71	1.79	1.81
Total	97.06	97.88	97.11	97.14	97.14	99.74
Si	6.43	6.67	6.44	6.53	6.51	6.43
Ti	0.06	0.08	0.11	0.12	0.15	0.16
Al	2.27	1.76	1.99	1.88	1.91	1.91
Cr	0.16	0.17	0.02	0.01	0.01	0.02
Fe^{+3}	0	0.01	0.22	0.18	0.17	0.25
Fe^{+2}	1.87	1.82	2.03	2.13	2.2	2.26
Mn	0.04	0.03	0.04	0	0.04	0.03
Mg	2.14	2.46	2.18	2.18	2.03	1.95
Ca	1.99	1.97	1.97	1.96	1.94	1.98
Na	0.35	0.28	0.36	0.34	0.3	0.31
K	0.43	0.35	0.34	0.33	0.35	0.35
Sum	15.74	15.6	15.7	15.65	15.62	15.65
Type	Pargasite	Edenite	Pargasite	Edenite	Ferro-edenite	Ferro-pargasite
X_{Mg}	0.53	0.57	0.52	0.51	0.48	0.46

Don: Donpeacorite

This is a preprint, the final version is subject to change, of the American Mineralogist (MSA)
Cite as Authors (Year) Title. American Mineralogist, in press.
DOI: https://doi.org/10.2138/am-2019-6811

Table 2. Representative compositional analyses of plagioclase and titanite from the host calc-silicate gneiss, quartzo-feldspathic pegmatitic vein and vesuvianite-garnet vein from the CGGC (stoichiometry of feldspar and titanite is calculated on the basis of 8 and 5 oxygens respectively).

Mineral	Plagioclase								
Rocktype	Host calc-silicate gneiss (AS32H1)		Quartzo-feldspathic pegmatitic vein (AS32Diii)				Vesuvianite-garnet vein (D4)		
Point no.	27 / 1.	25 / 1.	4 / 1.	8 / 1.	37 / 1.	41 / 1.	13 / 1.	29 / 1.	14 / 1.
Texture			Pl_1		Pl_2		Domain A	Domain B	Inclusions in Ves
SiO_2	54.1	45.82	48.06	52.48	53.56	62.96	42.9	42.93	44.18
TiO_2	0.02	0	0.03	0.01	0	0.03	0.01	0	0
Al_2O_3	29.36	34.72	32.54	29.53	28.23	21.73	35.42	35.77	35.94
FeO	0.09	0	0.14	0	0.05	0.62	0.15	0.08	0.07
MnO	0.03	0	0.02	0.12	0.01	0.1	0	0	0
MgO	0	0.01	0	0	0.01	0.37	0.01	0.01	0
CaO	12.18	18.75	16.28	12.92	11.76	3.27	21.23	21.3	19.53
Na_2O	4.48	1.01	2.62	4.23	4.75	9.41	0.7	0.4	0.38
K_2O	0.18	0.04	0.07	0.16	0.07	0.38	0.02	0	0.03
Total	100.45	100.35	99.76	99.45	98.44	98.87	100.44	100.49	100.13
Si	2.44	2.1	2.2	2.39	2.46	2.81	1.97	1.97	2.04
Ti	0	0	0	0	0	0	0	0	0
Al	1.56	1.88	1.76	1.59	1.53	1.14	1.92	1.94	1.95
Fe^{+3}	0	0	0.01	0	0	0.02	0.01	0	0
Fe^{+2}	0.01	0	0	0	0.01	0	0	0	0
Mn	0	0	0	0	0	0	0	0	0
Mg	0	0	0	0	0	0.02	0	0	0
Ca	0.59	0.92	0.8	0.63	0.58	0.16	1.04	1.05	0.97
Na	0.39	0.09	0.23	0.37	0.42	0.81	0.06	0.04	0.03
K	0.01	0	0	0.01	0	0.02	0	0	0
Total	5	5	5	5	5	5	5	5	5
An	0.59	0.91	0.77	0.62	0.58	0.16	0.94	0.97	0.96
Ab	0.4	0.09	0.22	0.37	0.42	0.82	0.06	0.03	0.03
Kfs	0.01	0	0	0.01	0	0.02	0	0	0

Mineral	Titanite						
Rocktype	Host calc-silicate gneiss (AS32H1)			Vesuvianite-garnet vein (D4)			
Point no.	4 / 1.	18 / 1.	22 / 1.	4 / 1.	50 / 1.	58 / 1.	43 / 1.
Texture	in matrix		Inclu.	Domain A		Domain B	
SiO_2	31.45	31.43	31.54	31.8	30.86	31.97	31.96
TiO_2	30.28	28.39	26.49	27.87	24.16	25.66	23.37
Al_2O_3	6.77	8.13	9.55	8.27	10.92	9.83	11.67
FeO	0.54	0.21	0.23	0.47	0.26	0.12	0.27
MnO	0.13	0.06	0	0.09	0.03	0.02	0
MgO	0.09	0.1	0.09	0.04	0.08	0.06	0.04
CaO	28.91	29.03	29.14	29.14	28.77	28.56	29.08
Na_2O	0	0.01	0.04	0.03	0.13	0.04	0.05
K_2O	0	0	0.01	0	0.03	0.01	0.03
F	2.49	1.74	2.08	2.11	2.65	3.45	1.86
Cl	0	0	0	0.04	0.01	0	0.02
Total	100.66	99.10	99.17	99.86	97.90	99.72	98.35
Si	1	1	1	1.01	0.99	1.02	1.01
Ti	0.73	0.68	0.63	0.67	0.58	0.62	0.56
Al	0.25	0.31	0.36	0.31	0.41	0.37	0.43
Fe^{+3}	0.01	0	0	0.01	0.01	0	0
Fe^{+2}	0	0	0	0	0	0	0
Mn	0	0	0	0	0	0	0
Mg	0	0	0	0	0	0	0
Ca	0.99	0.99	0.99	0.99	0.99	0.98	0.99
Na	0	0	0	0	0.01	0	0
K	0	0	0	0	0	0	0
Total	3	3	3	3	3	3	3
F	0.25	0.18	0.21	0.21	0.27	0.35	0.19
Cl	0.00	0.00	0.00	0.00	0.00	0.00	0.00
OH	0.00	0.13	0.15	0.10	0.14	0.02	0.24

This is a preprint, the final version is subject to change, of the American Mineralogist (MSA)
Cite as Authors (Year) Title. American Mineralogist, in press.
DOI: https://doi.org/10.2138/am-2019-6811

Table 3. Representative compositional analyses of vesuvianite and garnet in vesuvianite-garnet vein from CGGC (stoichiometry of vesuvianite is calculated on the basis of 50 cations; stoichiometry of garnet is calculated on the basis of 12 oxygens). Anions of vesuvianite calculated after the procedure of Ketcham (2015).

Mineral	Vesuvinite						Mineral	Garnet						
Point no.	17 / 1.	24 / 1.	42 / 1.	39 / 1.	6 / 1.	13 / 1.	Point no.	78 / 1.	7 / 1.	56 / 1.	57 / 1.	1//53	28 / 1.	38 / 1.
Texture	Domain A				Domain B2		Texture	Domain A		Domain B			Inclusion in domain A & B2	Ves in
SiO_2	36.86	35.52	36.93	36.89	36.42	36.05	SiO_2	38.71	38.43	38.96	38.64	38.72	38.84	38.98
TiO_2	1.48	1.29	1.58	1.21	1.22	1.26	TiO_2	0.28	0.29	0.23	0.29	0.4	0.18	0.31
Al_2O_3	15.78	16.82	15.65	16.18	16.41	15.83	Al_2O_3	20.41	19.04	20.49	19.28	19.41	20.31	20.09
Cr_2O_3	0.1	0.02	0.12	0.01	0.02	0.05	Cr_2O_3	0.29	0.31	0.01	0.45	0.39	0.43	0.34
Fe_2O_3	5.44	5.15	5.54	4.57	5.29	5.16	FeO	7.4	10.15	7.75	9.58	8.79	8.2	8.69
MnO	0.28	0.31	0.41	0.24	0.2	0.17	MnO	0.94	1.76	0.83	1.96	1.21	1.07	1.18
MgO	1.87	1.91	1.99	1.9	1.85	1.92	MgO	0.42	0.38	0.47	0.36	0.42	0.52	0.46
CaO	33.21	33.97	33.5	33.64	33.51	33.61	CaO	29.33	27.74	29.82	27.43	30.01	28.91	29
Na_2O	0.09	0.08	0.09	0.1	0.11	0.07	Na_2O	0.03	0.05	0.03	0.07	0.05	0.04	0.03
K_2O	0	0.02	0.02	0.04	0	0.02	K_2O	0.01	0.02	0.01	0.02	0	0	0.01
F	1.8	1.9	1.5	1.96	1.88	2.47	F	0.73	0.55	0.98	0.65	_	0.59	0.54
Cl	0.05	0.16	0.09	0.16	0	0								
Total*	96.96	97.15	97.42	96.9	96.91	96.75	Total	98.55	98.72	99.58	98.73	99.41	99.09	99.63
Si	18.52	17.78	18.42	18.51	18.26	18.23	Si	3.03	3.02	3.02	3.04	2.99	3.02	3.02
Ti	0.56	0.49	0.59	0.46	0.46	0.48	Ti	0.02	0.02	0.01	0.02	0.02	0.01	0.02
Al	9.34	9.92	9.2	9.57	9.7	9.44	Al	1.88	1.76	1.87	1.79	1.77	1.86	1.83
Cr	0.04	0.01	0.05	0	0.01	0.02	Cr	0.02	0.02	0	0.03	0.02	0.03	0.02
Fe^{+3}	2.06	1.94	2.08	1.73	1.99	1.97	Fe^{+3}	0.02	0.15	0.07	0.08	0.18	0.05	0.07
							Fe^{+2}	0.46	0.52	0.44	0.55	0.39	0.48	0.49
Mn	0.12	0.13	0.17	0.1	0.08	0.07	Mn	0.06	0.12	0.05	0.13	0.08	0.07	0.08
Mg	1.4	1.43	1.48	1.42	1.38	1.45	Mg	0.05	0.04	0.05	0.04	0.05	0.06	0.05
Ca	17.88	18.22	17.9	18.09	18	18.21	Ca	2.46	2.34	2.48	2.31	2.49	2.41	2.41
Na	0.09	0.08	0.09	0.1	0.11	0.07	Na	0	0.01	0	0.01	0.01	0.01	0
K	0	0.01	0.01	0.03	0	0.01	K	0	0	0	0	0	0	0
Total	50	50	50	50	50	50	Total	8	8	8	8	8	8	8
F	2.81	2.98	2.33	3.07	2.94	3.9	Adr	0.01	0.08	0.03	0.04	0.09	0.03	0.04
Cl	0.04	0.13	0.07	0.13	0	0	Prp	0.02	0.01	0.02	0.01	0.01	0.02	0.02
OH	6.15	5.88	6.59	5.8	6.06	5.1	Alm	0.15	0.16	0.14	0.17	0.12	0.15	0.16
$Al/Al+Fe^{+3}$	0.82	0.84	0.82	0.85	0.83	0.83	Grs	0.8	0.71	0.79	0.73	0.75	0.78	0.76
							Sps	0.02	0.04	0.02	0.04	0.02	0.02	0.02

* Concentration of boron is <20 ppm or less than the detection limit (2 ppm) of LA-ICP-MS

This is a preprint, the final version is subject to change, of the American Mineralogist (MSA)
Cite as Authors (Year) Title. American Mineralogist, in press.
DOI: https://doi.org/10.2138/am-2019-6811

Table 4. Characteristic invariant points and univariant reactions for topology I and II. The reactions are also marked in terms of the absent phases (within parenthesis).

Topology	Characteristic invariant points	Characteristic univariant reactions
Topology I	[Cal Wo]	Qtz Zo Ves=Di Grs (Cal, Wo, An)
	[An Wo]	Di Zo Cal Grs=Ves (Wo, Qtz, An)
	[Qtz Wo]	Di Zo Grs= Ves An (Wo, Qtz,Cal)
Topology II	[Wo Zo]	Di Qtz Cal An=Ves (Wo, Zo, Grs)
	[Grs Wo]	

964

Figure 1

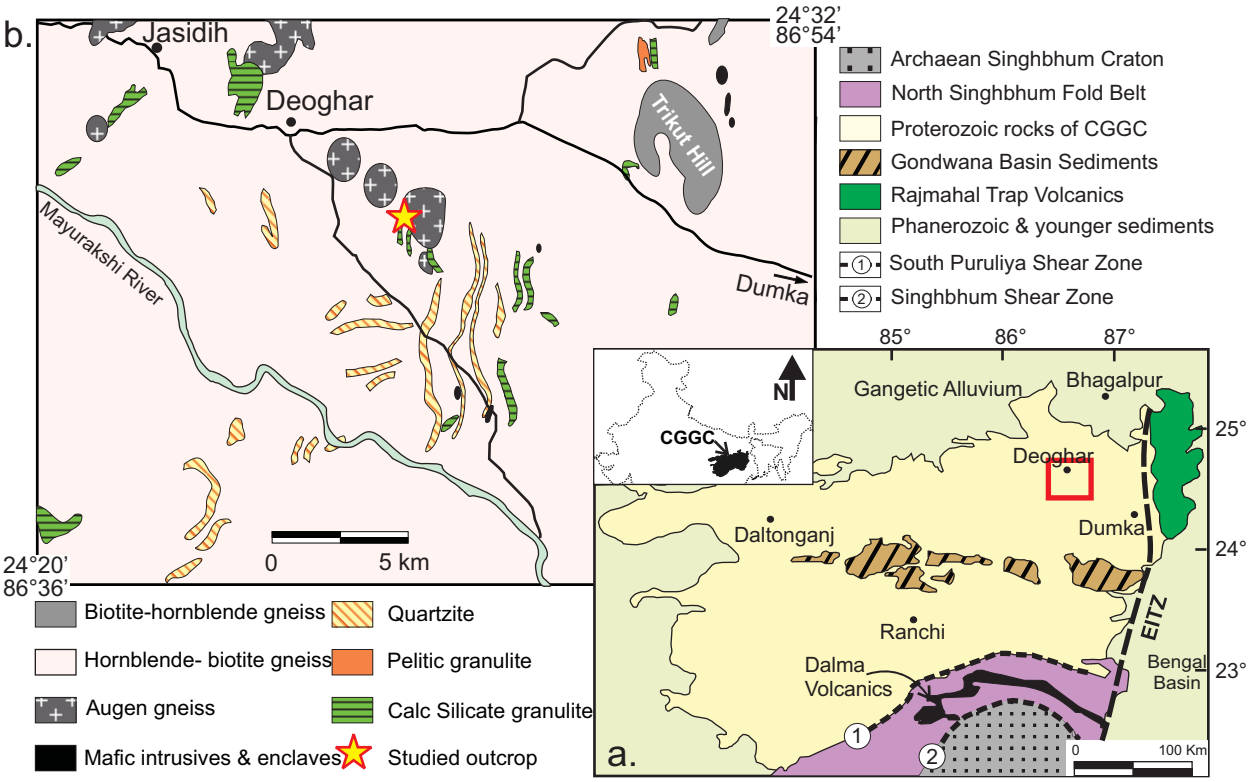
b.
Jasidih
Deoghar
Trikut Hill
Mayurakshi River
Dumka
24°32'
86°54'
24°20'
86°36'
0
5 km
Archaean Singhbhum Craton
North Singhbhum Fold Belt
Proterozoic rocks of CGGC
Gondwana Basin Sediments
Rajmahal Trap Volcanics
Phanerozoic & younger sediments
South Puruliya Shear Zone
Singhbhum Shear Zone
Biotite-hornblende gneiss
Hornblende- biotite gneiss
Augen gneiss
Mafic intrusives & enclaves
Quartzite
Pelitic granulite
Calc Silicate granulite
Studied outcrop
85°
86°
87°
N
CGGC
Gangetic Alluvium
Bhagalpur
Deoghar
Dumka
Daltonganj
Ranchi
Dalma
Volcanics
EITZ
Bengal
Basin
25°
24°
23°
a.
0
100 Km

Figure 2

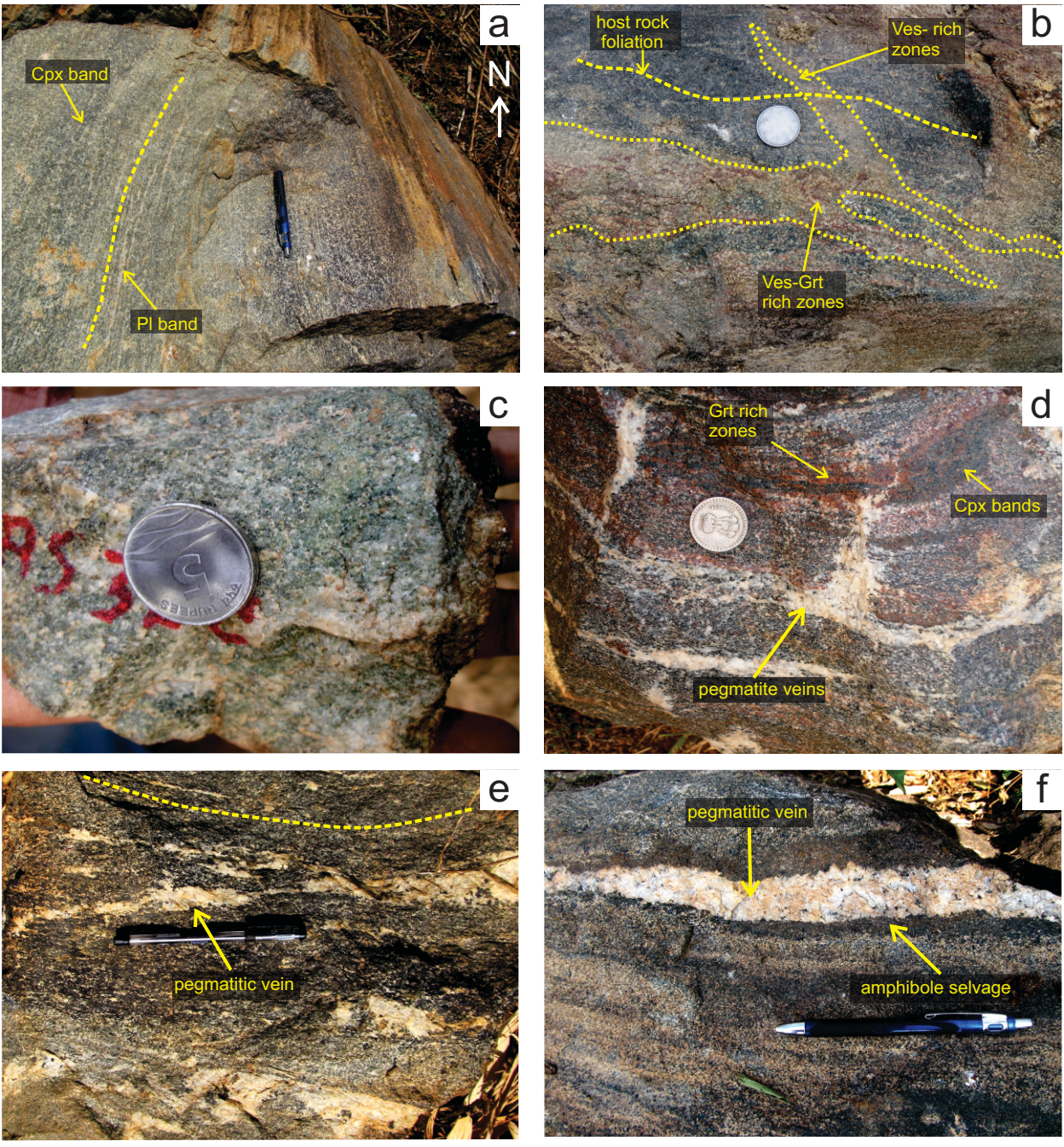
a
Cpx band
Pl band
N
b
host rock foliation
Ves- rich zones
Ves-Grt rich zones
c
d
Grt rich zones
Cpx bands
pegmatite veins
e
pegmatitic vein
f
pegmatitic vein
amphibole selvage

Figure 3

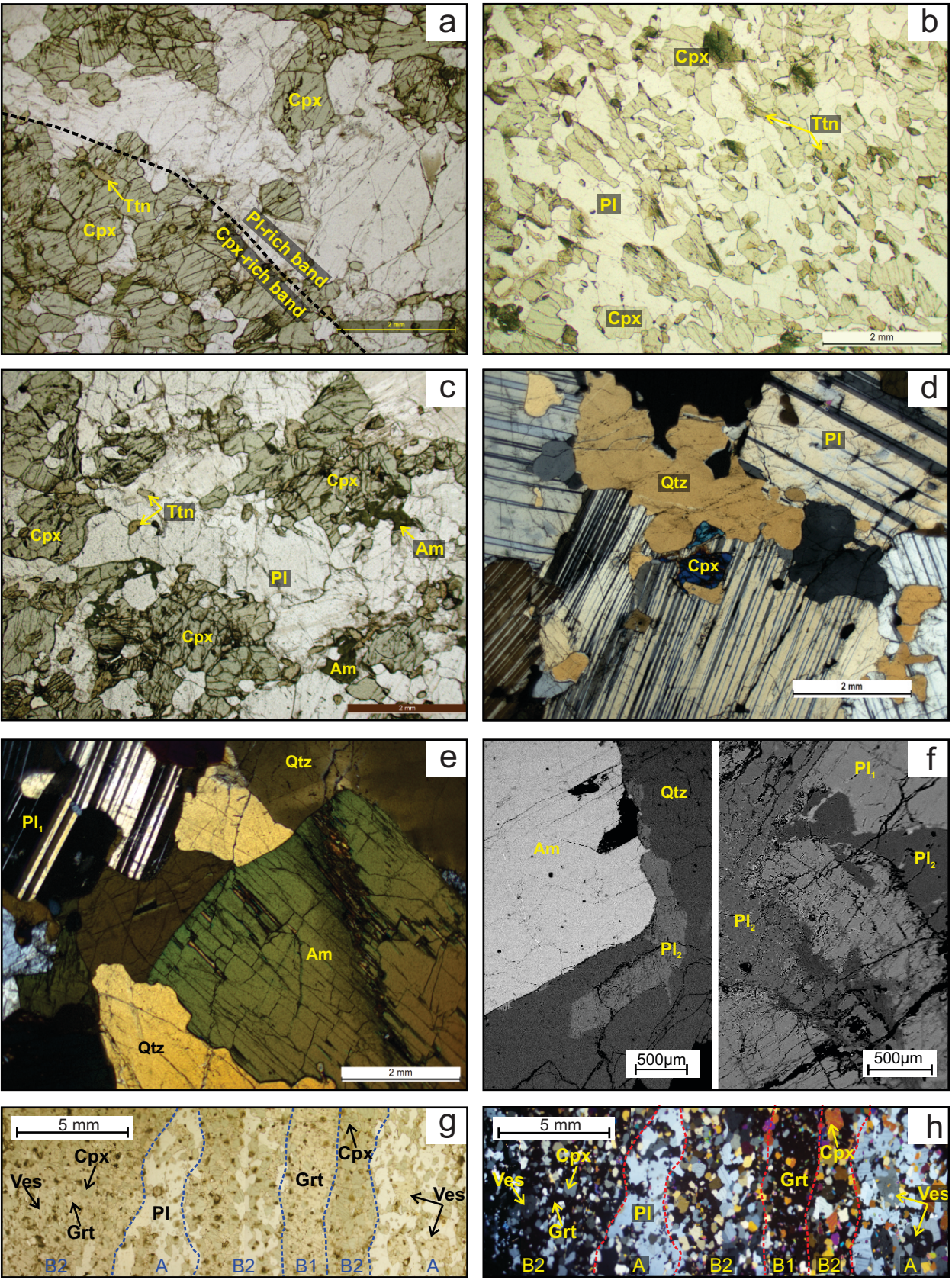
a
Cpx
Ttn
Cpx
Pl-rich band
Cpx-rich band
2 mm
b
Cpx
Ttn
Pl
Cpx
2 mm
c
Cpx
Ttn
Cpx
Am
Pl
Cpx
Am
2 mm
d
Pl
Qtz
Cpx
2 mm
e
Qtz
Pl1
Am
Qtz
2 mm
f
Qtz
Am
Pl2
500µm
Pl1
Pl2
Pl2
500µm
g
5 mm
Cpx
Ves
Grt
Pl
Grt
Cpx
Ves
B2
A
B2
B1
B2
A
h
5 mm
Cpx
Ves
Grt
Pl
Grt
Cpx
Ves
B2
A
B2
B1
B2
A

Figure 3 cont.

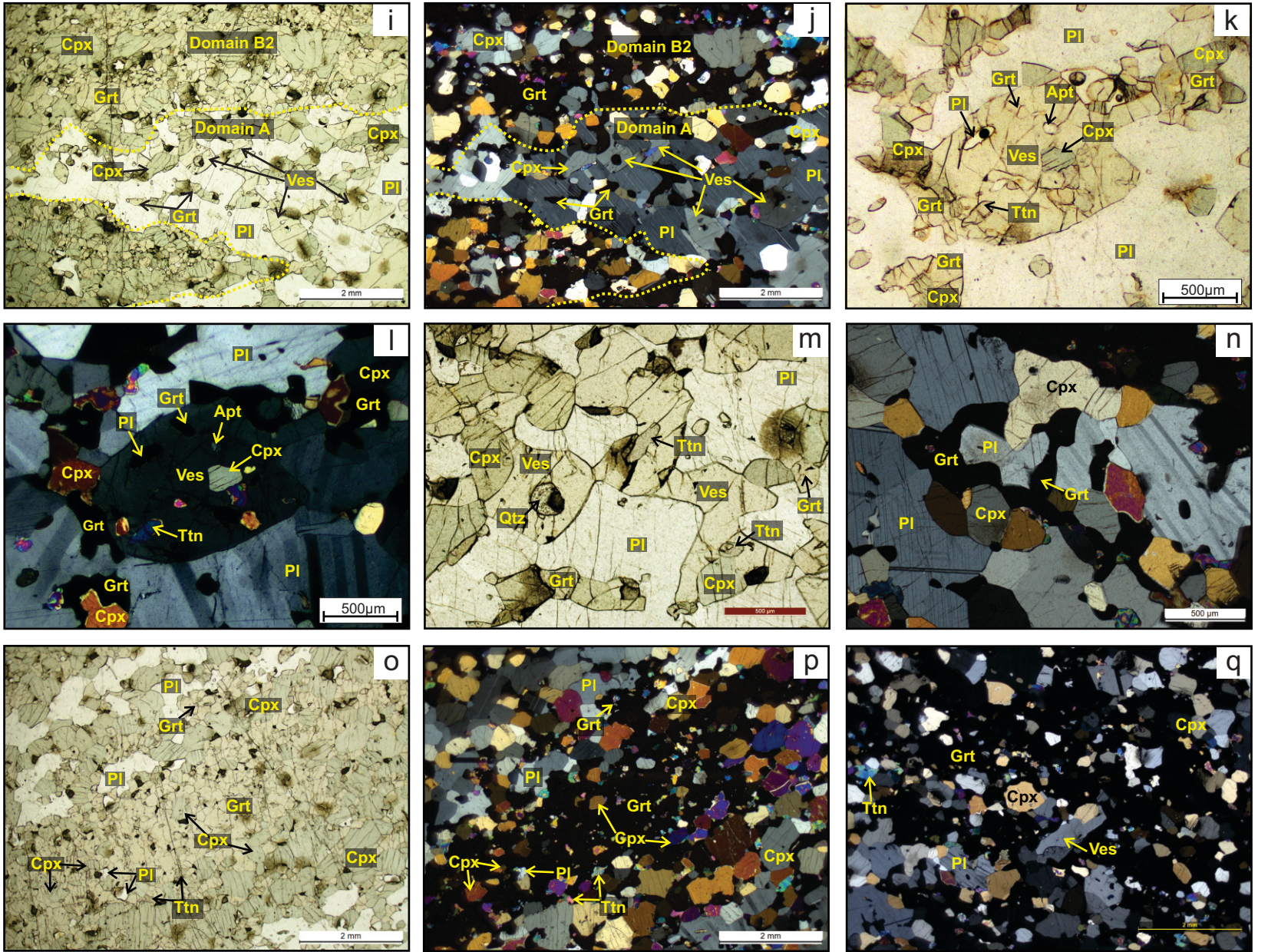

Figure 4

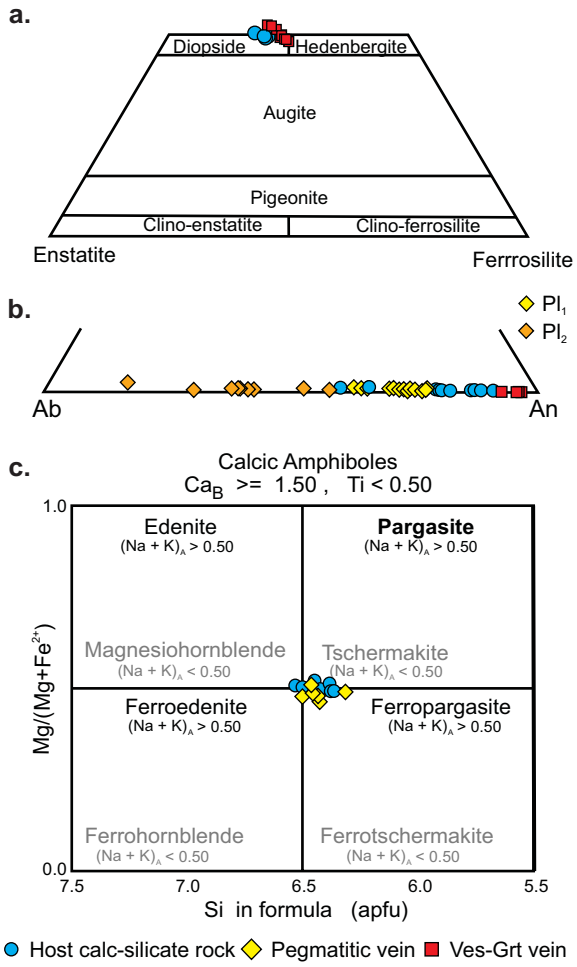
a.
Diopside
Hedenbergite
Augite
Pigeonite
Clino-enstatite
Clino-ferrosilite
Enstatite
Ferrrosilite
b.
Pl1
Pl2
Ab
An
c.
Calcic Amphiboles
CaB >= 1.50 , Ti < 0.50
Edenite
(Na + K)A > 0.50
Pargasite
(Na + K)A > 0.50
Magnesiohornblende
(Na + K)A < 0.50
Tschermakite
(Na + K)A < 0.50
Ferroedenite
(Na + K)A > 0.50
Ferropargasite
(Na + K)A > 0.50
Ferrohornblende
(Na + K)A < 0.50
Ferrotschermakite
(Na + K)A < 0.50
Mg/(Mg+Fe2+)
1.0
0.0
7.5
7.0
6.5
6.0
5.5
Si in formula (apfu)
Host calc-silicate rock
Pegmatitic vein
Ves-Grt vein

Figure 5

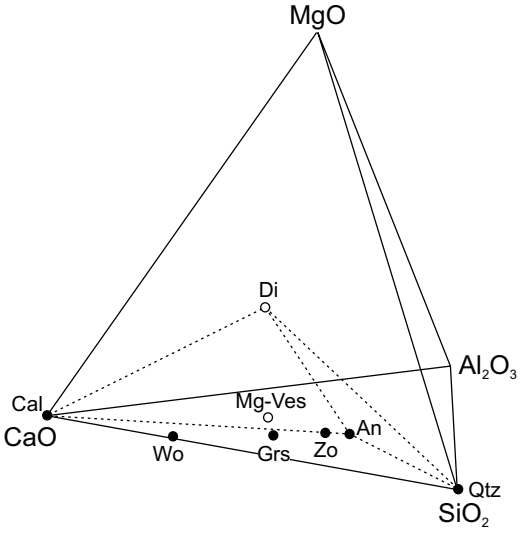

Figure 6

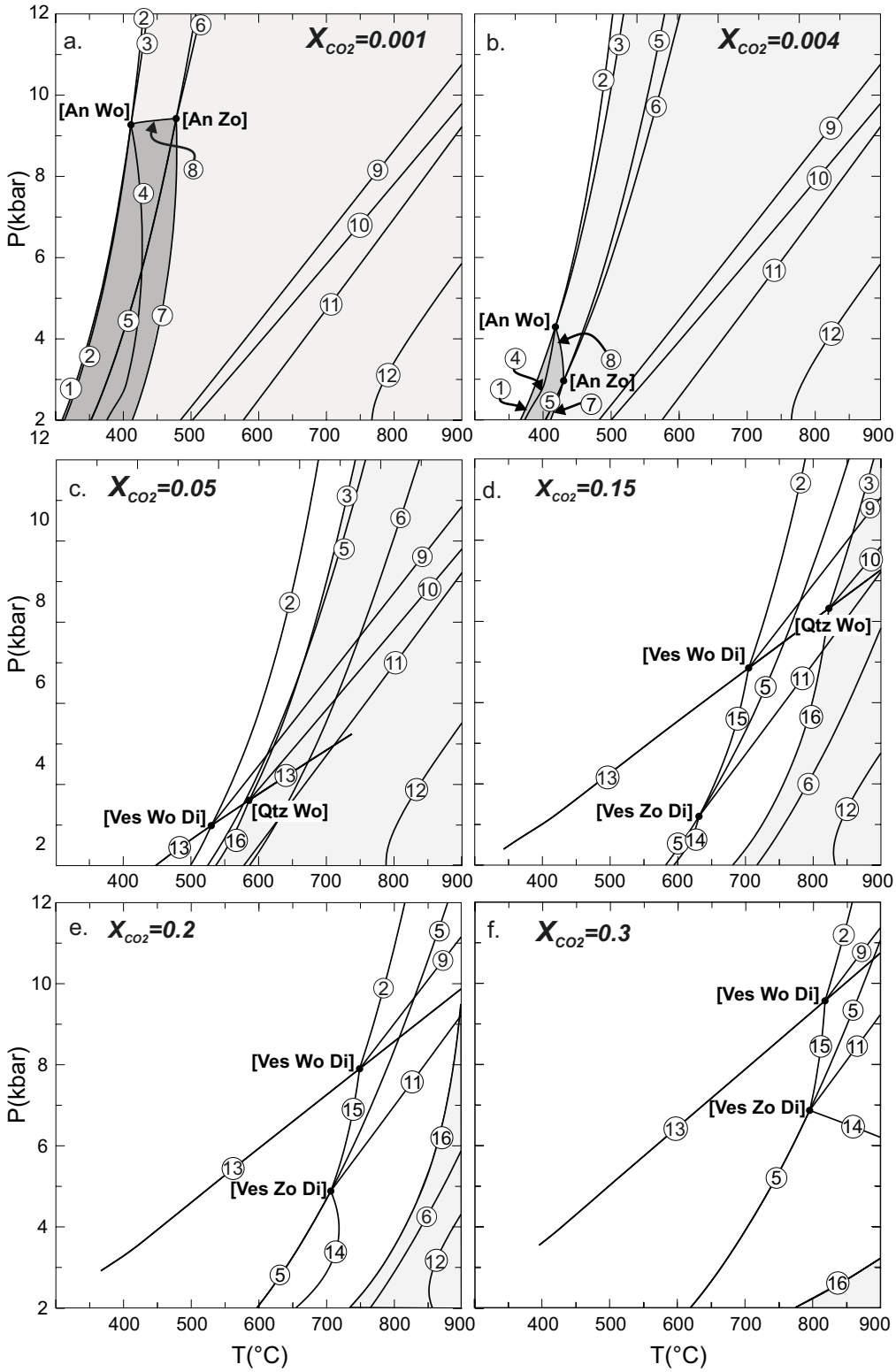

1. Cal Di Zo Qtz = Ves
2. Cal Zo Qtz = Grs
3. Cal Di Zo Grs = Ves
4. Zo Qtz Ves = Di Grs
5. Cal Qtz = Wo
6. Cal Di Grs = Ves Wo
7. Ves Qtz = Di Wo Grs
8. Di Cal Grs= Qtz Ves
9. Qtz Zo = An Grs
10. Di Grs Zo = An Ves
11. Grs Qtz = An Wo
12. Di Grs = An Ves Wo
13. Zo = Cal An
14. Cal Wo An = Grs
15. Cal Qtz An = Grs
16. Cal Di An Grs = Ves

Figure 7

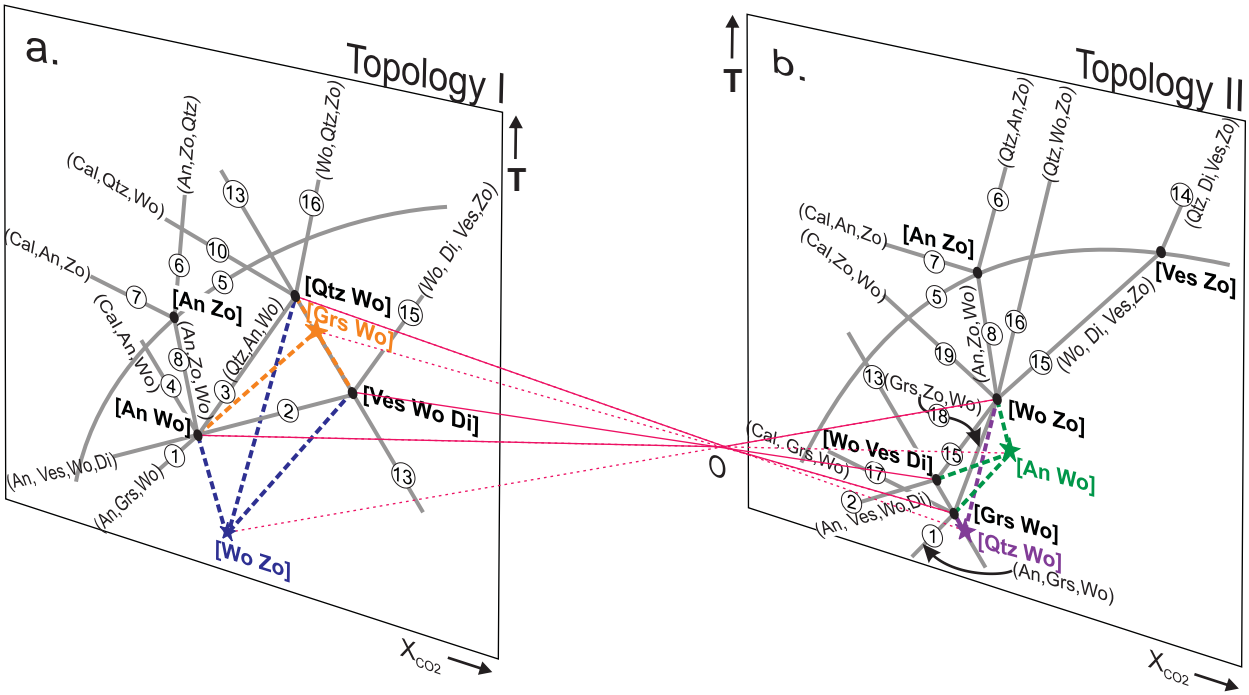

(1) $4Zo+6Di+16\ Cal+3Qtz+4H_2O = 3Ves+16CO_2$
(2) $2Zo+5Cal+3Qtz = 3Grs+5CO_2+H_2O$
(3) $3Grs+6Di+2Zo+11Cal+5H_2O = 3Ves+11CO_2$
(4) $5Ves+11Qtz+4Zo = 16Grs+10Di+12H_2O$
(5) $Cal+Qtz = Wo$
(6) $2Grs+2Di+3Cal+2H_2O = Ves+Wo+3CO_2$
(7) $Ves+3Qtz = 2Grs+2Di+2Wo+2H_2O$
(8) $2Grs+2Di+2Cal+2H_2O = Ves+Qtz+2CO_2$

(10) $Grs+2Di+8Zo = Ves+11An+2H_2O$
(13) $2Zo+CO_2 = 3An+Cal+H_2O$
(14) $Cal+An+Wo = Grs+CO_2$
(15) $2Cal+An+Qtz = Grs+2CO_2$
(16) $Grs+2Di+An+4Cal+2H_2O = Ves+4CO_2$
(17) $2Di+Qtz+12Zo+2H_2O = Ves+16An+4H_2O$
(18) $2Di+Qtz+6Cal+2An+2H_2O = Ves+6CO_2$
(19) $Ves+2Qtz+2An = 3Grs+2Di+2H_2O$

Figure 8a

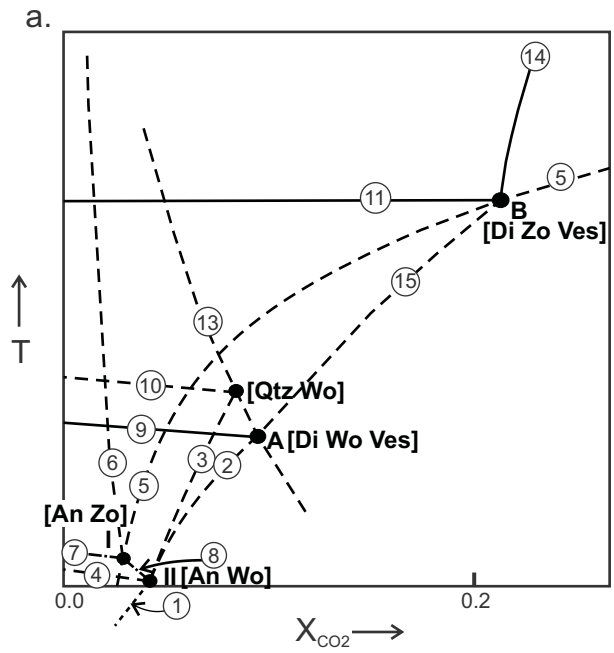

Reaction equations are written with the high temperature assemblage to the right of the = sign

1. Zo Di Cal Qtz = Ves
2. Qtz Cal Zo = Grs
3. Di Cal Grs Zo = Ves
4. Ves Zo Qtz = Di Grs
5. Qtz Cal = Wo
6. Di Cal Grs= Wo Ves
7. Ves Qtz = Di Grs Wo
8. Qtz Ves = Di Cal Grs
9. Qtz Zo = An Grs
10. Di Grs Zo = Ves An
11. Qtz Grs = An Wo
12. Di Grs = An Ves Wo
13. Zo = An Cal
14. An Cal Wo = Grs
15. An Qtz Cal = Grs
16. Di Cal Grs An = Ves

Figure 8 b-e

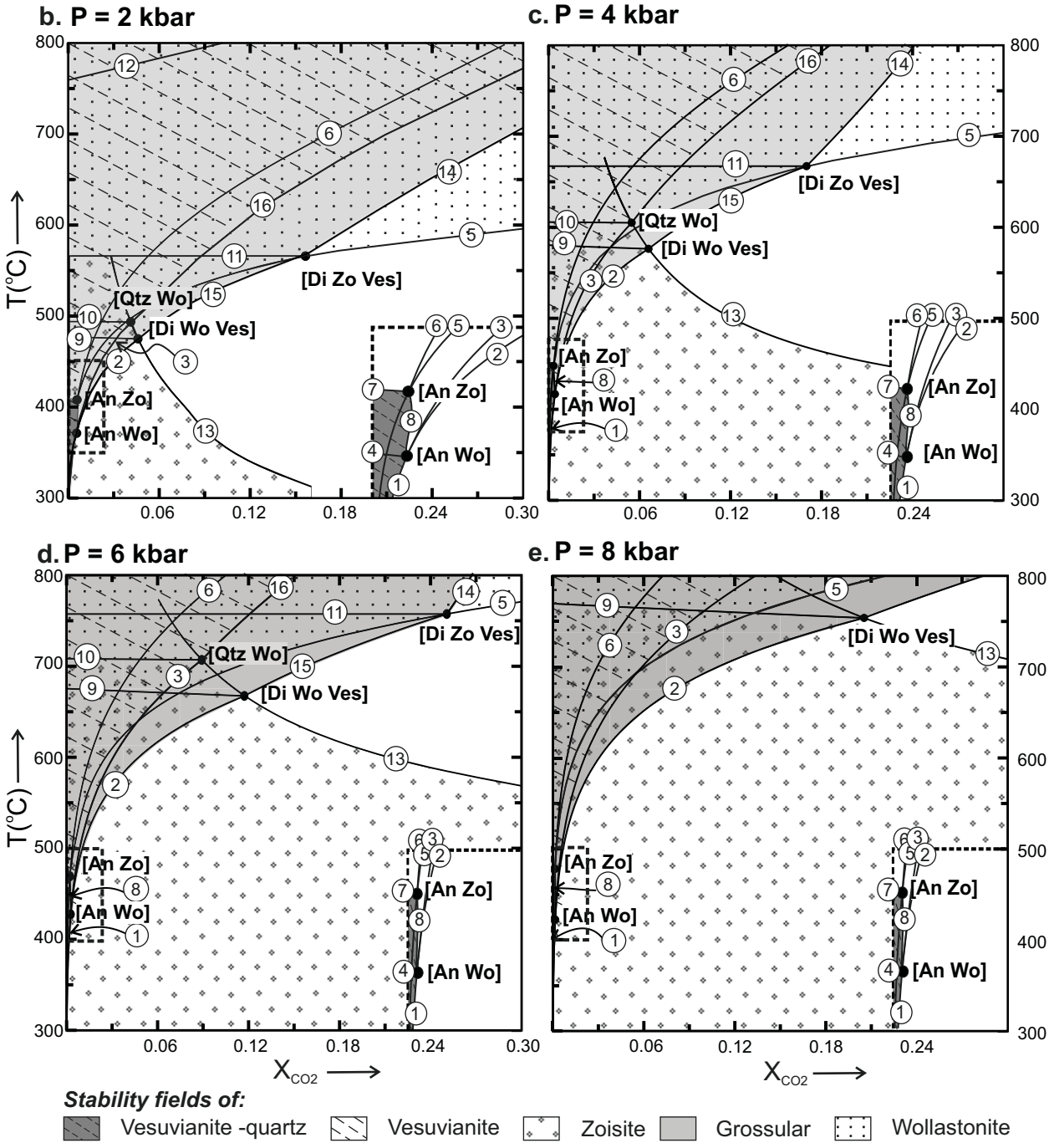
b. P = 2 kbar
c. P = 4 kbar
d. P = 6 kbar
e. P = 8 kbar
T(°C)
X_{CO2}
[Qtz Wo]
[Di Wo Ves]
[Di Zo Ves]
[An Zo]
[An Wo]
Stability fields of:
Vesuvianite -quartz
Vesuvianite
Zoisite
Grossular
Wollastonite

Figure 9

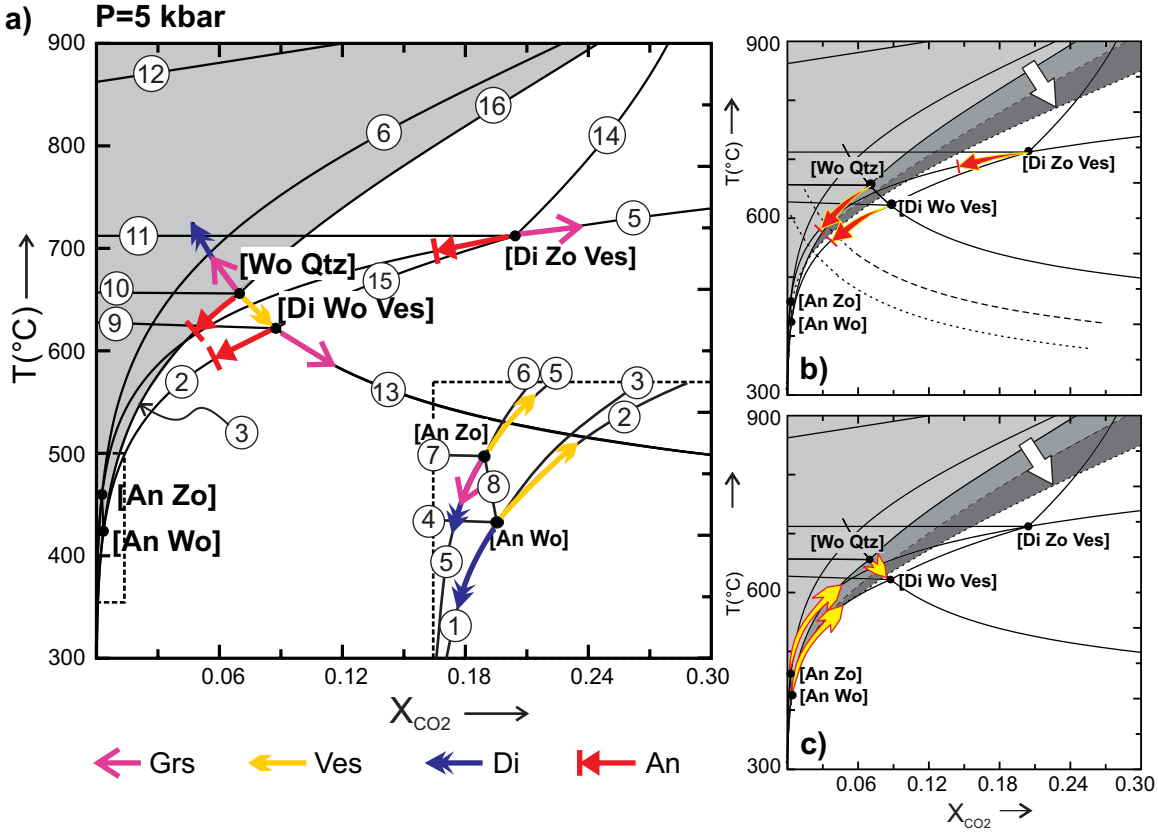
a)
P=5 kbar
T(°C)
X_{CO2}
[Wo Qtz]
[Di Wo Ves]
[Di Zo Ves]
[An Zo]
[An Wo]
Grs
Ves
Di
An
b)
c)

Figure 10 a

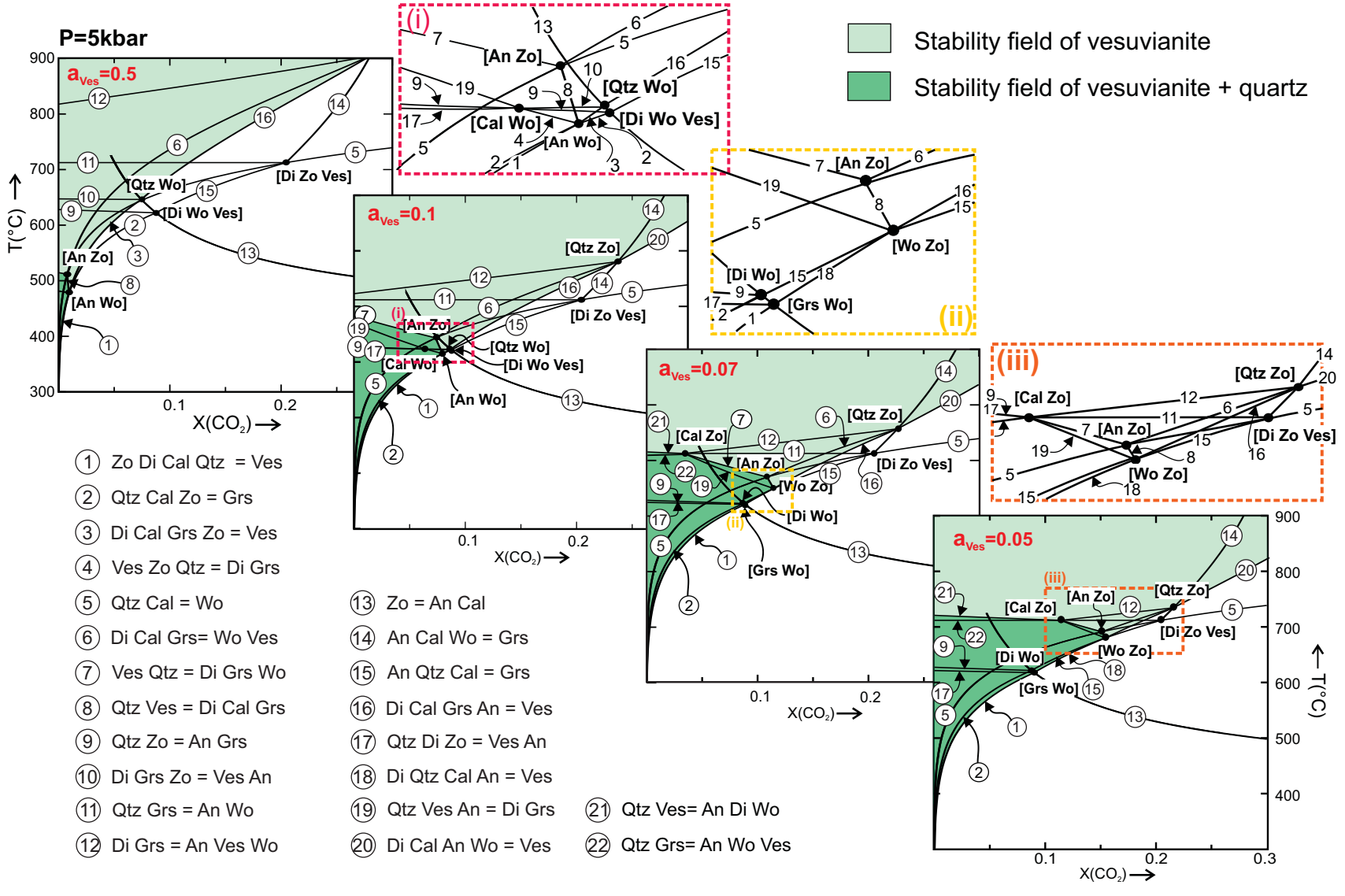
P=5kbar
Stability field of vesuvianite
Stability field of vesuvianite + quartz
a_{Ves}=0.5
a_{Ves}=0.1
a_{Ves}=0.07
a_{Ves}=0.05
T(°C)
X(CO$_2$)
[An Zo]
[An Wo]
[Qtz Wo]
[Di Wo Ves]
[Di Zo Ves]
[Cal Wo]
[Qtz Zo]
[Cal Zo]
[Wo Zo]
[Di Wo]
[Grs Wo]
(i)
(ii)
(iii)
1 Zo Di Cal Qtz = Ves
2 Qtz Cal Zo = Grs
3 Di Cal Grs Zo = Ves
4 Ves Zo Qtz = Di Grs
5 Qtz Cal = Wo
6 Di Cal Grs= Wo Ves
7 Ves Qtz = Di Grs Wo
8 Qtz Ves = Di Cal Grs
9 Qtz Zo = An Grs
10 Di Grs Zo = Ves An
11 Qtz Grs = An Wo
12 Di Grs = An Ves Wo
13 Zo = An Cal
14 An Cal Wo = Grs
15 An Qtz Cal = Grs
16 Di Cal Grs An = Ves
17 Qtz Di Zo = Ves An
18 Di Qtz Cal An = Ves
19 Qtz Ves An = Di Grs
20 Di Cal An Wo = Ves
21 Qtz Ves= An Di Wo
22 Qtz Grs= An Wo Ves

Figure 10 b

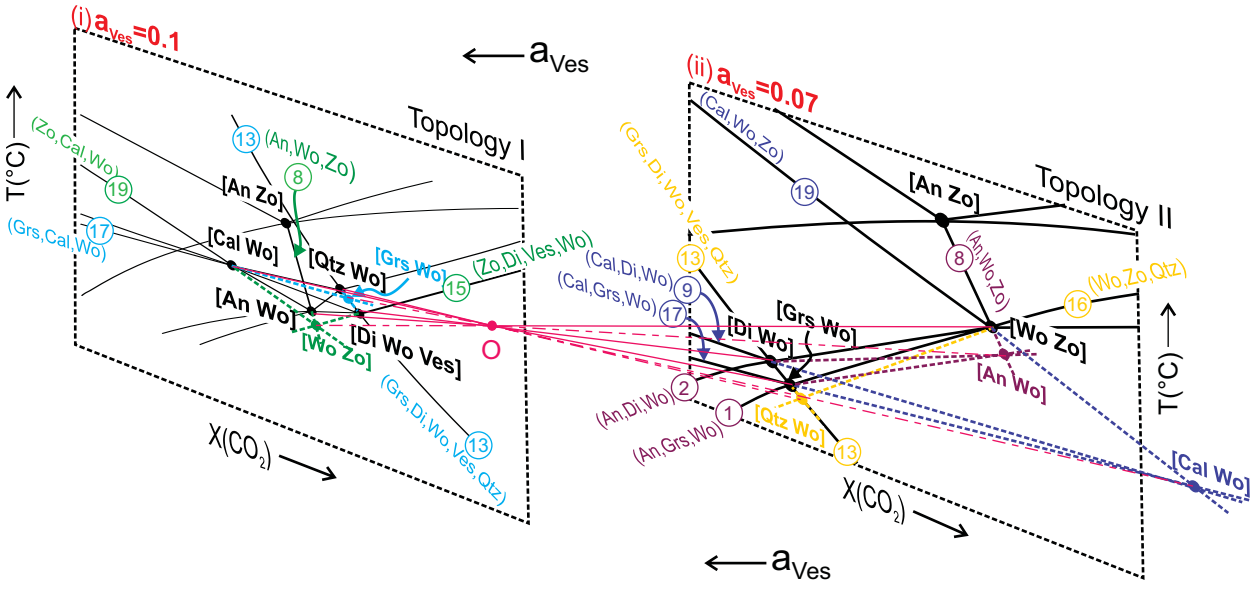
(i) a_{Ves}=0.1
a_{Ves}
Topology I
T(°C)
(Zo,Cal,Wo)
19
13
(An,Wo,Zo)
8
[An Zo]
17
(Grs,Cal,Wo)
[Cal Wo]
[Qtz Wo]
[Grs Wo]
(Zo,Di,Ves,Wo)
15
[An Wo]
[Wo Zo]
[Di Wo Ves]
O
(Grs,Di,Wo,Ves,Qtz)
13
X(CO2)
(ii) a_{Ves}=0.07
(Cal,Wo,Zo)
19
[An Zo]
Topology II
(Grs,Di,Wo,Ves,Qtz)
13
(An,Wo,Zo)
8
(Cal,Di,Wo)
9
(Cal,Grs,Wo)
17
[Di Wo]
[Grs Wo]
[Wo Zo]
16
(Wo,Zo,Qtz)
T(°C)
[An Wo]
(An,Di,Wo)
2
(An,Grs,Wo)
1
[Qtz Wo]
13
X(CO2)
[Cal Wo]
a_{Ves}

Figure 11

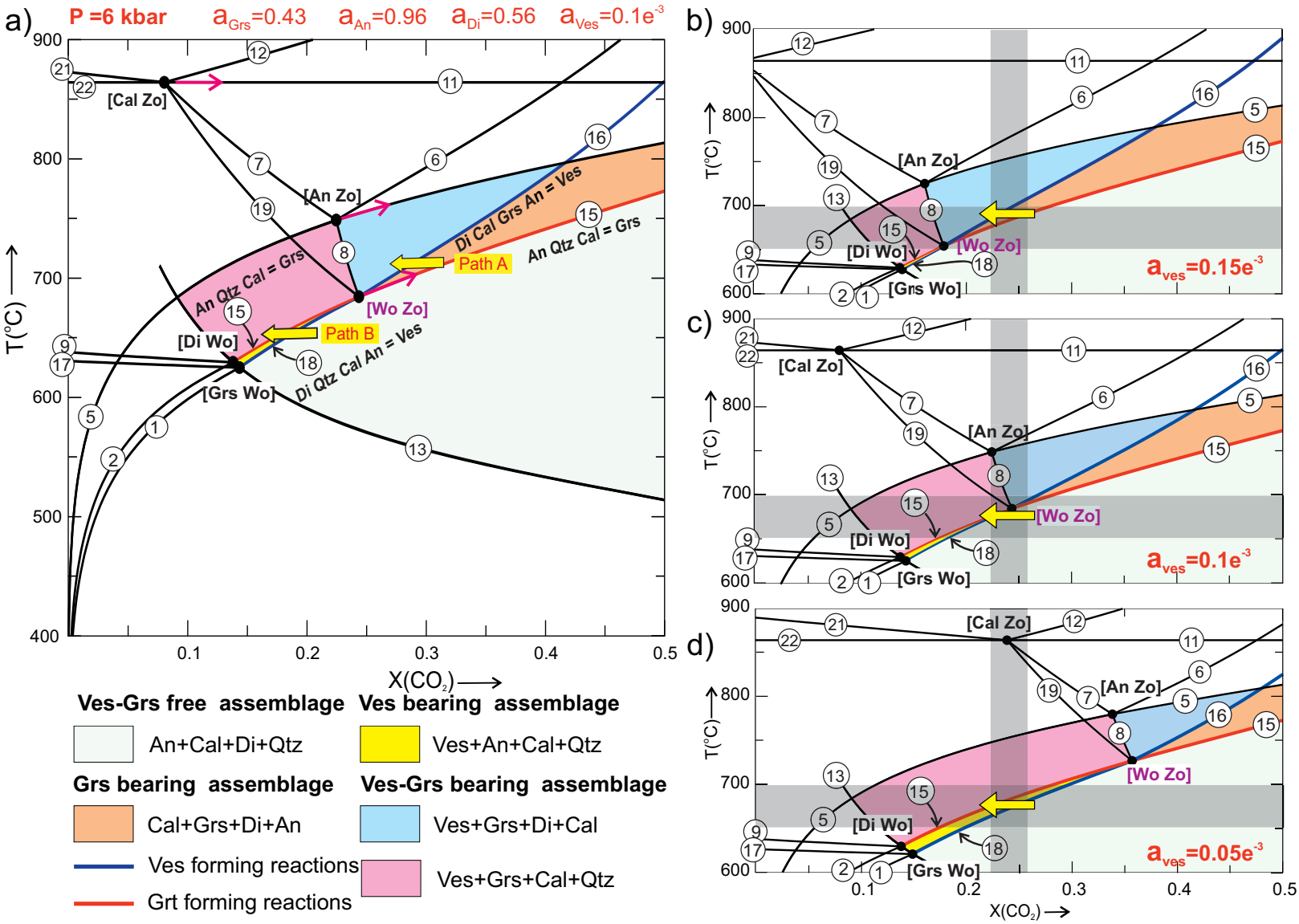
a)
P =6 kbar
a_{Grs}=0.43
a_{An}=0.96
a_{Di}=0.56
a_{Ves}=0.1e^{-3}
T(°C)
X(CO$_2$)
[Cal Zo]
[An Zo]
[Wo Zo]
[Di Wo]
[Grs Wo]
Path A
Path B
An Qtz Cal = Grs
Di Cal Grs An = Ves
Di Qtz Cal An = Ves
b)
a_{ves}=0.15e^{-3}
c)
a_{ves}=0.1e^{-3}
d)
a_{ves}=0.05e^{-3}
Ves-Grs free assemblage
An+Cal+Di+Qtz
Ves bearing assemblage
Ves+An+Cal+Qtz
Grs bearing assemblage
Cal+Grs+Di+An
Ves-Grs bearing assemblage
Ves+Grs+Di+Cal
Ves forming reactions
Grt forming reactions
Ves+Grs+Cal+Qtz